Frequency Modulation Spectroscopy of the "Forbidden" M1 & E2 1283nm Transition in Thallium

by
Christopher D. Holmes

A thesis submitted in partial fulfillment
of the requirements for the
Degree of Bachelor of Arts with Honors
in Astrophysics

WILLIAMS COLLEGE
Williamstown, Massachusetts
May 26, 2003

Abstract

We present progress towards the first direct measurements of the isotope shift, Stark shift and Stark induced amplitudes in the $6P_{1/2} \rightarrow 6P_{3/2}$ transition in thallium. The weak nature of this "forbidden" M1 and E2 transition requires a new RF detection technique called "two-tone" spectroscopy, which we describe here. Using a vapor cell, we demonstrate that our detection apparatus has adequate sensitivity for measurements in the atomic beam. Precision measurements of atomic structure, such as these, provide strict tests of wavefunction calculations and electroweak physics, important steps in the ongoing efforts to refine the Standard Model and understanding of atomic properties.

Contents

List of Figures

List of Tables

Chapter 1

Once Upon a Time– An Introduction

Dorada, Shangrilo;
Lederman, Yang, Lee, Wu
studied a parity
unconcerned force;

verified amply, though
counterintuitive,
'lectroweak physics lacks
symmetry's source.[1]

"*Once upon a time...*" hardly sounds like the opening words of a scientific treatise, but that is where I would like to begin— in a realm far away from the everyday realities of our laboratory, in the land where physicists dream of where their work may someday lead.

Physics moves in two directions: inward and outward. The outward direction is perhaps the aspect of physics most similar to other sciences. In this vein we apply known rules of material interactions to explain and understand the behavior of larger systems. On the other hand, many physicists direct their thoughts towards ever smaller, more autonomous entities. Herein lie the specialties of particle physics and musings about a "final theory." Of course, most research does not fall neatly into one category or the other and ours is no exception.

This work deals with the electronic structure of thallium, specifically measurements of the energies of its electron configurations both with and without the influence of static electric fields. As an atomic system, the valence structure of thallium

[1]The poems introducing each chapter are Double-Dactyls, a contrived, but harmless verse form. Some of the many rules are that: each line must be a double-dactyl; the second line of the first stanza must be a name; somewhere in the second stanza there must be a single double-dactyl word; the first line must be nonsense and the last lines of the two stanzas must rhyme. It is an open question whether these rules of poetry or the multipole transition selection rules appear more arbitrary, even capricious, to the uninitiated.

has been known for many years, but the complexity of 81 electrons and protons plus 124 (or 122) neutrons makes calculating wavefunctions more than a formidable computational problem. While we can write down the Hamiltonian for such complicated systems, single-electron atoms are the only atomic systems for which the Schrödinger Equation is analytically soluble, and even these wavefunctions must be approximated when one includes the complexities of relativity, quantum field theory and the weak interaction. For more complex atoms there are techniques to predict wavefunctions, but the best of these approximations still have errors of at least several percent. By improving the precision of experimental data, we provide standards for evaluating the success of competing theoretical wavefuctions and calculational approaches. Accuracy in predicting thallium's electronic structure improves one's proficiency in predicting others. In this sense our work is part of the "outward" goal of using quantum mechanics to explain a greater diversity of atoms in hopes that we might better predict the atomic and chemical properties of the entire periodic table.

An equal component of our long-term motivation for this work derives from the opposite tendency of physicists to think about the "fundamental" constituents of matter. Particle physics is often considered synonymous with high-energy physics, but we daily prove that wrong. Physicists labor under the assumption that the laws governing one system should hold in all others, and so it is with particle accelerators, the canonical domain of particle physics, and every atom in the universe. By compensating in precision and sensitivity for what lose by working at low energies, we can probe the same electroweak interactions that occur in accelerators costing thousands of times as much as our laboratory; however, we must disentangle the electroweak physics from the complex interactions of myriad non-fundamental particles found in atoms. A still more exotic motivation for our breed of atomic spectroscopy is the search for physics "beyond" the standard model. The origins of mass and the cause of symmetry breaking are two of the biggest open problems for particle physicists. While we have no expectation that our work will resolve those questions, it will place additional constraints on what these new physical laws might be, but who can say when or where the unknown will next reveal itself? Thus our work is part of the ongoing development of the standard model and the physics governing the most basic components of our universe.

Dreaming of how our work relates to the next Nobel Prize or the next revolution in physics aside, what we do in the laboratory, and what I shall focus on here, is measure the atomic structure of the thallium's $6P_{1/2}$ and $6P_{3/2}$ states. Using a new method of "two-tone spectroscopy" we have achieved a new level of sensitivity which will allow us in the near future to measure the isotope shift (between ^{203}Tl and ^{205}Tl), Stark shift and Stark induced amplitudes in transitions between the various hyperfine states under investigation.

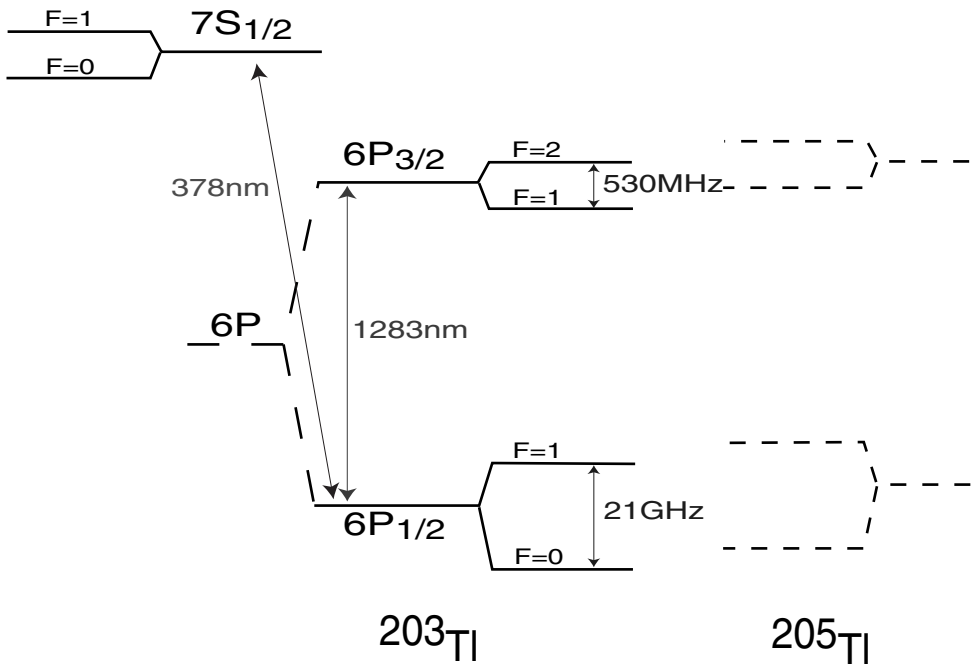

Figure 1.1: Valence electron states for thallium, including hyperfine splitting and isotope shifts.

1.1 Parity in the Standard Model

In this complex world of ours, physicists are especially fond of the symmetries that simplify our understanding of it. For centuries if not millennia, scientists have known that experiments and the physical laws that underlie them are reproducible when conducted at different times and places. These symmetries of translation through time, space and rotation give rise to the conservation laws of energy, linear momentum and angular momentum. In contrast with these continuous symmetries, there are discrete symmetries of time (T), charge (C) and parity (P) inversion that have a more tortuous historical relationship to theory. These symmetries express the belief that if time were reversed ($t \rightarrow -t$) or positive and negative charges interchanged or coordinates inverted ($x \rightarrow -x, y \rightarrow -y, z \rightarrow -z$) then the same physical laws should be true. Classical physics physics supported those assumptions, but it wasn't until 1927 that Wigner proved that the symmetry of the Coulomb potential requires that parity be conserved through electromagnetic interactions. At that point all known theories were consistent with the discrete symmetries.

In 1956 and 1957 the orthodoxy of symmetry was overthrown when Yang and Lee proposed a solution to the nagging paradox of the decay of the τ and θ particles (now known as the single K meson), a solution that implied parity was not conserved in the weak interaction ([LY56]). They proposed further experiments that would test the validity of parity conservation and soon thereafter the first experimental test, a study of the β^- decay of Cobalt-60, confirmed that parity was indeed violated in the weak

interaction ([WA57]). That experiment showed that decaying atoms preferentially emit left-handed electrons regardless of the orientation of the nuclear spin. The concept of parity non-conservation (PNC) became ensconced in the later unification of the electromagnetic and weak forces, two manifestations of a single electroweak interaction. Experiments and theorists soon discovered that each of the other symmetries were violated as well, but together their product is conserved (CPT).[2] In the ensuing decade, the Standard Model of particle physics emerged as an amalgamation of Quantum Electrodynamics (QED, theory governing interactions via the electroweak force) and Quantum Chromodynamics (QCD, theory governing interactions via the strong nuclear force), together with the properties of all known particles. This model is a seminal achievement of modern physical theory and today remains astonishingly successful.

1.2 Parity Violation in Thallium

Measurements of parity violation in atoms have a history going back to the initial discovery of PNC, but new measurements continue to have relevance today. The early experiments, such as those conducted by Wu et al, focused on decay processes; these events are mediated by the $W^{\pm}$ particles. In the 1970s, theory predicted that even stable atoms should be influenced by the weak interaction, via the massive Z^0 boson. This particle affects both nucleons and electrons in a phenomenon known as a "weak neutral current" because the Z^0, which has no charge, is exchanged or"flows" between the nucleus and nearby electrons. Present day experiments focus on obtaining experimental values for the weak charge (Q_W), a quantity that determines the magnitude of PNC and contains information about nuclear structure, but is exogenous to electroweak theory. This constant, together with $C(Z)$, a function containing information about electron wavefunctions, determines the size of PNC effects in atoms according to

$$\varepsilon_{PNC} = C(Z) * Q_W. \tag{1.1}$$

In neutral atoms, the energy corrections due to PNC are small in comparison with the electromagnetic interactions that dominate within atoms. The reason is that the Z^0 boson which mediates the weak interaction in stable atoms is extremely heavy (91GeV/c^2 or 89m_p); by the energy-time uncertainty principle the Z^0 must be very short lived and therefore have a very short range (approximately 10^{-18}m, see [Nic98]), meaning that only electrons penetrating the nucleus could be affected by this interaction. Thus the heavier elements with larger nuclei containing more nucleons are the only ones that exhibit measurable PNC effects. The relationship between $\varepsilon_{PNC}, C(Z)$

[2]The weak interaction is the only source of these discrete symmetry violations. Experiments and theory agree that gravity, electromagnetism and the strong nuclear force all conserve C,P and T, individually as well as collectively. Future tests in our lab, as well as others, will put greater limits on the size of possible discrete symmetry violations. Our lab, among others, is working on an experiment to test these conservation laws more precisely.

	Group	Experimental Precision	Theoretical Wavefunction Precision
Cs	Colorado '97	0.35%	1%
Tl	U.W. '95	1.2%	2.5% [KPJ01]
Pb	U.W. '93	1.2%	8%
Bi	Oxford '91	2%	8%

Table 1.1: Current experimental (ε_{PNC}) and theoretical (C(Z)) results pertinent to Q_W determinations. (from [Dor02])

and atomic number is

$$\varepsilon_{PNC} \propto Z^3 * f(Z), \tag{1.2}$$

where $f(Z)$ is a small numerical factor of order unity. This indicates that one should look for PNC effects in heavier elements, but this is precisely where $C(Z)$ is difficult to calculate, so extracting a value for Q_W is harder.

As a compromise between the difficulties of measuring PNC and the tribulations of calculating $C(Z)$, several atomic systems have become popular. Wavefunction calculations need to be accurate to within one percent for measurements of Q_W to be meaningful. To date cesium has given the most stringent tests of experimental and theoretical agreement because, as an alkali metal, cesium's single valence electron makes the atom "hydrogenic." Thallium is another attractive proving ground for PNC tests because it is "almost hydrogenic." With one valence p electron, thallium is slightly more complex than the alkalis, but still much simpler than most elements. Lead and Bismuth provide greater theoretical challenges, so the error in these calculations is greater, but continually shrinking. Table 1.1 shows the current status of experimental and theoretical results concerning PNC.

The weak force and its signature parity violation manifest themselves in atomic systems in several ways. Firstly, it shifts the energy levels of electron states. In thallium this happens because each state mixes with states of the opposite parity. (e.g. $6P_{1/2}$, an odd state mixes with even S states as shown in Figure 1.2) While these energy shifts are not themselves measurable because we have nothing to compare them to, the mixing does allow new transitions which were not previously possible, shown as "PNC-E1" in the figure. This additional transition amplitude causes interference among the transition pathways and rotates the plane of polarized light transmitted through a thallium sample. In cesium, there are *tons* of atomic structure and PNC measurements of remarkable accuracy because of the relative ease of working with this element, but the experimental results for thallium are more sparse. Our lab has made several measurement of thallium's structure and one of the PNC induced optical rotation. In an experiment completed by Leo Tsai, the polarization rotation was on the order of milliradians, ([Tsa98], [MT99]); although small, this is still many orders of magnitude larger than it would be for light atoms.

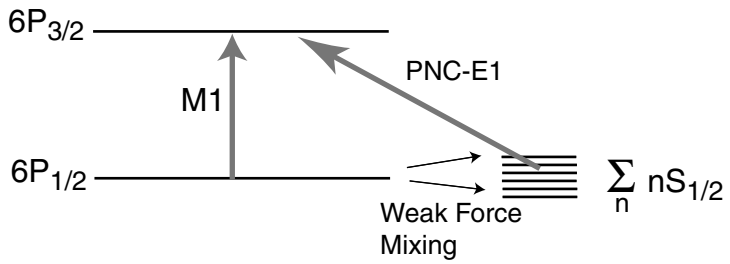

Figure 1.2: The mixing of S and P states via the weak interaction.

1.3 Parity Conserving Physics in Thallium

In terms of electroweak physics, the value of optical rotation measurements are limited by the precision of theoretical wavefunction approximations. As Equation 1.1 shows, uncertainty in the value of Q_W comes from both the experimental uncertainty in measurements of ε_{PNC} as well as the theoretical uncertainty in calculating $C(Z)$. Independent precise experimental results are helpful in refining the wavefunction calculations. There are bountiful measurements one could make to verify a proposed set of wavefunctions. In particular, measurements of the hyperfine energies reflect information about nuclear structure as well as the behavior of electrons in and near the nucleus. The same goes for the isotope shifts, which are due to differences in nuclear configuration as well as a reduced mass effect. Stark shifts and Stark induced transition amplitudes encapsulate information about the overlap integrals between different orbitals. Many potential measurements in thallium or other elements, if done with sufficient precision, could be used to test the agreement of theory with reality. Each of these structure measurements are complementary because they involve distinct sums over wavefunctions (call these $D(Z)$, $F(Z)$, $G(Z)\ldots$), similar to $C(Z)$. If theoretical wavefunctions and experiments give consistent values for D, G, and F, then one will have greater confidence in the accuracy of $C(Z)$ and therefore Q_W. Our group has made many such measurements and continues this project in the present work.

Recent results from our laboratory include a measurement of the isotope shift in the $6P_{1/2} \rightarrow 7S_{1/2}$ transition ([RLM00]) as well as the stark shift in the same transition ([DFS02], [Dor02]). Note that these results do not directly concern the $6P_{1/2} \rightarrow 6P_{3/2}$ transition in which a PNC effect has been measured for thallium. Nevertheless those experiments were significant in part because they probed the $7S_{1/2}$ state, the state that mixes most with the $6P_{1/2}$state due to the weak interaction. In addition, the great precision of these measurements exceeds that of wavefunction calculations for thallium, providing a target for theorists to hit.

1.3.1 Present Work

Our current experimental work deals with the PNC $6P_{1/2} \rightarrow 6P_{3/2}$, measuring new atomic structure parameters, including isotope shifts and eventually Stark shifts and

Stark amplitudes. Direct measurements of these quantities have not been completed before, however indirect measurements of the isotope shift have already come from the $6P_{1/2} \rightarrow 7S_{1/2}$ and $6P_{3/2} \rightarrow 7S_{1/2}$ transitions. There is some inconsistency in the results from two such indirect measurements ([Her93],[RLM00]), so our work should resolve this discrepancy. This will be a significant result because previous PNC measurements in this transition used the inferred isotope shift as a given quantity in order to extract ε_{PNC}. An error in the isotope shift would propagate to an error in the magnitude of PNC. We take advantage of the narrow absorption features within the atomic beam unit, compared with the vapor cell, to refine our understanding of absorption profiles and their electric field induced changes. However, we must also contend with the low beam density coupled with the inherent weakness of the magnetic dipole (M1) and electric quadrupole (E2) transitions that we are studying. Together these effects require a new, more sensitive detection method.

In case you skipped the table of contents, here's what is in store for you. You're already done with Chapter one; good for you. Now comes the fun stuff. Chapter two explains much of the atomic physics that governs the structure of thallium. It also discusses the laser interaction and the sorts of features that appear in a spectrum. Chapter three is about the "two-tone" modulation technique that we employ to improve the sensitivity of our apparatus. It presents general background on frequency modulation as well as details specific to our setup. In Chapter four, I introduce the laboratory equipment that gives life to the ideas laid out in the previous two chapters. Finally, I present some of our recent data and discuss the future of this project.

Chapter 2

Atomic Physics

Slipandry-Puffildrip;
Particle theorists,
working with nuclear
scientists, who

make perturbations
relativistically,
calculate wavefunctions
better than you.

As is well known to students of physics at all levels, atoms are full of complexity. With 81 electrons, a large nucleus and two prevalent isotopes, thallium is no exception. While it would be nice to conduct tests of the standard model in simple atomic systems like hydrogen, the electroweak effects of interest are only measurable in heavier elements because the strength of these interactions scales with the atomic number cubed. In this chapter, I discuss some of the complexities of these heavy atoms and the nature of the transitions we study.

2.1 Thallium Valence Structure

This section and the following discussion of selection rules are an extended explanation of Figure 2.1. Throughout this section, referring to the diagram of thallium's energy states may be helpful.

2.1.1 Fine Structure

There is nothing surprising about thallium's fine structure, except perhaps its size. In hydrogen, the $2P_{1/2}and2P_{3/2}$ energy levels are separated by approximately 10GHz (and the effect is smaller for higher n values). In contrast, the fine-structure splitting of thallium's 6P states corresponds to a frequency of $2.3 \cdot 10^5$GHz, or a wavelength of 1283nm. In both elements electron spin-orbit coupling is responsible for lifting

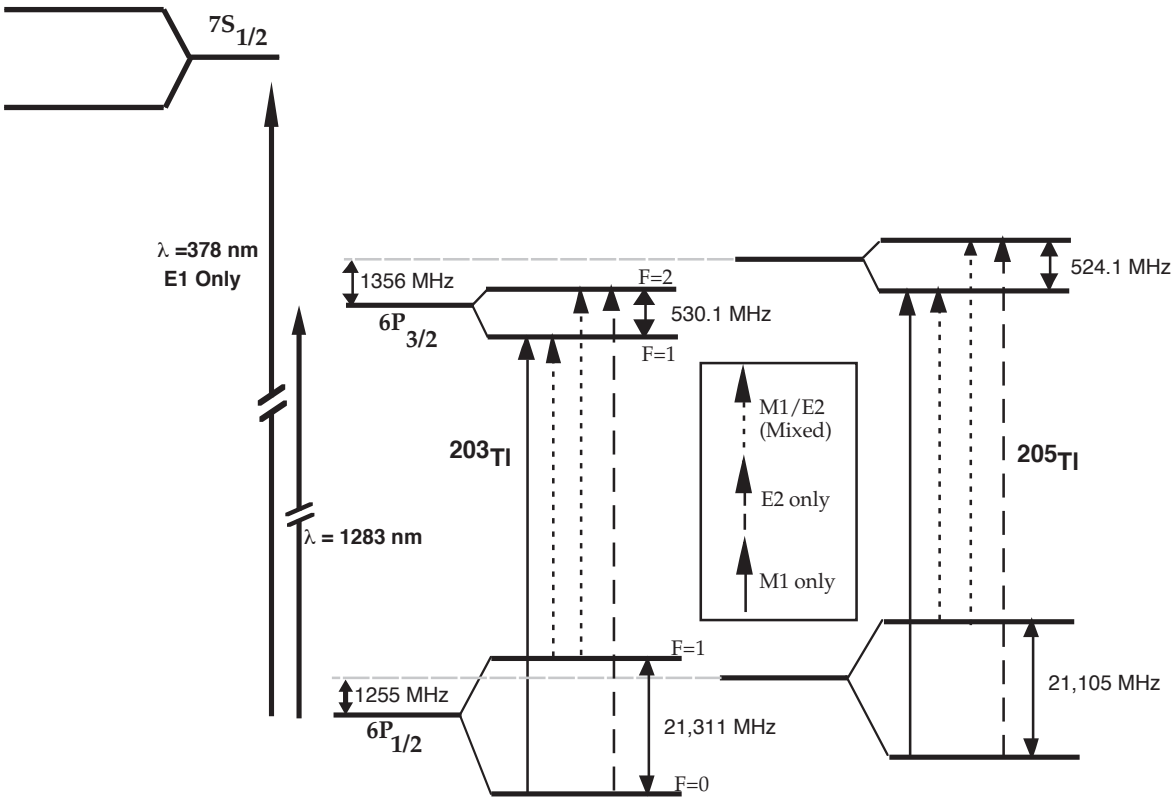

Figure 2.1: Low lying energy levels in thallium and transitions amongst them. [Maj03]

the degeneracy of the electron spin orientation. The primary cause for the radical difference in the magnitudes of fine structure lies with relativistic quantum theory. After solving the (non-relativistic) Schrodinger equation, one can make a relativistic energy correction, but this affects all orbitals with the same n value equally, so this cannot affect the fine structure splitting. (See [Gri95] for example.) The fully relativistic Dirac equation makes more drastic changes to the orbital wavefunctions. The solutions to this equation tell us that the $6P_{1/2}$ orbital assumes more character of an S state than does the $6P_{3/2}$ state. Specifically, a $6P_{1/2}$ electron has a much greater probability of being inside or near the nucleus. Inside the electron cloud, the unshielded nucleus increases the electron's binding energy, shifting the $6P_{1/2}$level down in energy significantly and increasing to the large fine structure. On a smaller energy scale, the nuclear size and configuration also perturb the $6P_{1/2}$electron to a greater degree than they affect the $6P_{3/2}$state.

2.1.2 Hyperfine Structure

In some sense we are lucky that thallium's hyperfine structure is as simple as it is. Within the nucleus, the spins of all protons and neutrons are antiparallel, except for one, giving a total nuclear spin of 1/2. The consequence of this is that each fine structure state splits into exactly two hyperfine states.

The magnitudes of the hyperfine splittings for the $6P_{1/2}$and $6P_{3/2}$states are quite disparate. For comparison, in the hydrogen ground state, the hyperfine splitting is at the famous frequency of 1.42GHz, a value midway between those for the thallium 6P states. Like the fine structure magnitudes, the hyperfine energies are also related to the degree of penetration into the electron cloud for each orbital. Since the $6P_{1/2}$wavefunction has significant amplitude inside the electron cloud, it sees an unshielded nucleus and it velocity expectation value is much higher. These factors increase the strength of the magnetic field coupling the electron and the nucleus. In contrast, the $6P_{3/2}$electron sees a much smaller nuclear charge and moves slowly, both of which diminish the coupling magnetic field. Therefore it makes sense that the $6P_{1/2}$state should have a greater hyperfine splitting (21GHz compared with 530MHz). Incidently, hydrogen also fits this rhetorical model. In that element, the electron sees the full nuclear charge and has significant probability of entering the nucleus, but the nuclear charge is so much smaller that the hyperfine energy lies between those of thallium's 6P states.

From here, we can understand the absorption spectrum of the 1283nm transition. Figure 2.1 shows the hyperfine structure of the $6P_{1/2}$ and $6P_{3/2}$ states, with all of the allowed excitations indicated by arrows. In the absence of hyperfine structure, the energy levels of the two thallium isotopes are not quite equal. The isotope shifts for each fine structure state, in combination with slightly different hyperfine splittings, gives rise to eight transitions at slightly different frequencies. Figure 2.2 displays the cumulative absorption cross section with correct relative strengths. The linewidths are what we expect to see in the atomic beam apparatus. Note that the eight absorption features fall into two groups, separated by approximately 21GHz (the $6P_{1/2}$hyperfine splitting). Those on the left all start at the $6P_{1/2}$ F=1 state. These absorptions are stronger than those initiated from the F=0 state for two reasons. 1) The F=1 state is triply degenerate ($m_F = 0, \pm 1$), so there are three times as many atoms in this state as in the non-degenerate F=0 state ($m_F = 0$). 2) All transitions from the F=1 state involve both M1 and E2 mechanisms, whereas transitions from F=0 involve only one mechanism or the other, because of selection rules explained below in Section 2.2. Note that all $6P_{1/2}$ states (one F=0 state and 3 degenerate F=1 states) should be almost equally populated according to Boltzmann statistics. The energy difference between these states is $\sim 10^{-4}$eV, well below the average energy per degree of freedom at the operating temperature of our experiment. Thus the transition amplitudes are not appreciably affected by a Boltzmann population distribution.

Looking closely at each of the hyperfine groups individually, we see that the absorption frequency is slightly different for the two isotopes. As mentioned earlier, the difference in frequency is due to the slightly different isotope shifts for the 203 and 205 isotopes. The difference in amplitude of the absorptions is entirely due to the relative abundance of the two isotopes. Thallium occurs naturally with 70.5% in the ^{205}Tl isotope; therefore absorption strength for this isotope is slightly more than twice that of ^{203}Tl. The origin of the isotope shift lies within the nucleus. Measurements of this shift can therefore test the accuracy of nuclear models.

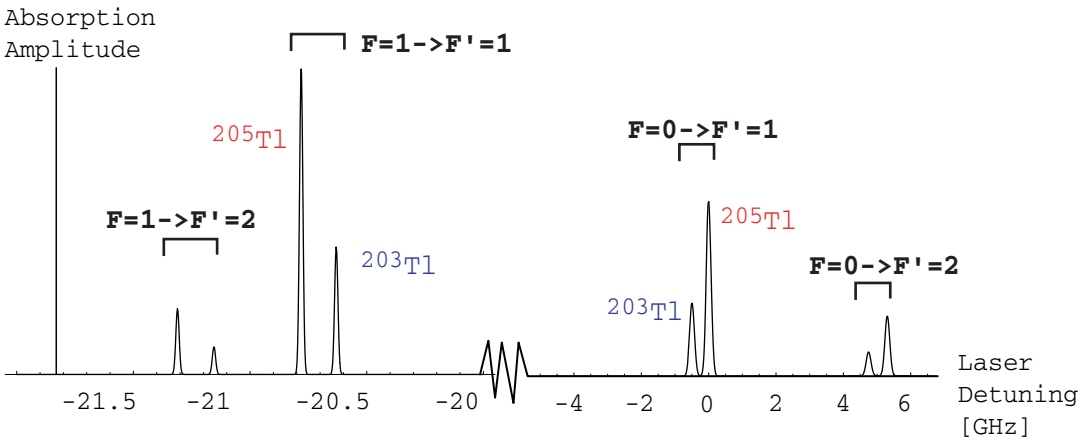

Figure 2.2: Absorption spectrum of $6P_{1/2} \rightarrow 6P_{3/2}$ transition, with appropriate relative amplitudes and Doppler widths comparable to measurements in the atomic beam.

2.2 The Meaning of "Forbidden"

In everyday quantum mechanics, whatever that might be, transitions between two p orbitals are "forbidden." This is because the selection rules for an electric dipole (E1) transition, the strongest of the light-induced variety, require that $\Delta l = \pm 1$ (also $\Delta m_l = 0, \pm 1$, while Δn is unrestricted). Despite the word "forbidden" emblazoned upon the $6P_{1/2} \rightarrow 6P_{3/2}$ transition, I hope you, dear reader, will not despair, nor proclaim this thesis a sham, for yea their are more things in heaven and earth than electric dipole transitions. Light is an electro*magnetic* wave and indeed the magnetic field produces *magnetic* dipole (M1) transitions between the $6P_{1/2}$ and $6P_{3/2}$ states. There is still another kind of transition that appears in this work: the electric quadrupole (E2) transition. In fact there are higher orders of multipoles as well, but these become increasingly less likely to occur and so we can disregard them. A more precise way to think about these higher order multipole transitions is as successive approximations to the interaction Hamiltonian. A plane wave polarized in the $\vec{\epsilon}$ direction and travelling along $\vec{r}$ can stimulate a transition between states $|\psi_a\rangle$ and $|\psi_b\rangle$ if and only if

$$\langle \psi_b | H' | \psi_a \rangle \neq 0, \tag{2.1}$$

where

$$H' = \vec{d} \cdot \vec{E} = \vec{d} \cdot \hat{\epsilon} E_0 e^{i\omega t - i\vec{k}\cdot\vec{r}}. \tag{2.2}$$

If the wavelength of the radiation is much longer than the size of the atom, then one can approximate $e^{i\vec{k}\cdot\vec{r}}$ as 1, meaning that we assume the electric field is constant across the atom. This leads to the dominant E1 transitions, while higher order approximations lead to other kinds of transitions. The successive corrections take into consideration the magnetic field of the EM wave as well the gradient of the electric field.

Rule	Electric Dipole	Magnetic Dipole	Electric Quadrupole
Δn	Unrestricted	0	Unrestricted
Δl	± 1	0	0, ± 2
Δm_l	0, ± 1	0, ± 1	0, ± 1, ± 2
Δm_s	0	0, ± 1	0
Δj	0, ± 1	± 1	0, ± 1, ± 2
ΔF	0, ± 1	0, ± 1	0, ± 1, ± 2
Δm_F	0, ± 1	0, ± 1	0, ± 1, ± 2
Other			$F + F' \geq 2$

Table 2.1: Selection rules for atomic transitions, using "good" and "bad" quantum numbers.

One can derive the selection rules for any order of magnetic or electric multiple by finding the states $|\psi_a\rangle$ and $|\psi_b\rangle$ that satisfy Equation 2.1. The selection rules are generally derived for the $n, l, m_l, s, m_s, I, m_I$ quantum numbers, then converted to selection rules for the "good" quantum numbers n, j, F, m_F using Clebsch-Gordon coefficients for decomposition. Derivations of these rules exist in many books, at least in part. ([Cor86] is especially thorough and [CDL77] is especially clear.) I summarize the results of these calculations in Table 2.1.[1] In all cases the selection rules for the m's are determined by the polarization of the laser relative to the quantization axis. Note the special restriction on E2 that the sum of the initial and final total atomic angular momentum numbers must be at least two for such a transition to occur. This is due to the tensor structure of the quadrupole operator. The arrows in Figure 2.1 show the implications of these selection rules for the $6P_{1/2}$ and $6P_{3/2}$ transitions.

You may wonder why the phrase "forbidden transition" exists at all if there are so many exotic possibilities for moving amongst atomic states. The reason is that the E1 interaction is so much stronger than the others that we can ignore the others in most situations. It is a mistake, however, to think that "forbidden" transitions are unusual. In a terrestrial setting, most atoms will lose energy through collisions before decaying by an M1 or M2 pathway, but in space it's a different story. The rarified environment makes collisions between atoms unlikely, so even slow transitions have plenty of time to occur. Indeed the 21cm M1 emission is a common means of mapping hydrogen distribution throughout our galaxy and beyond. Closer to home, non-E1 transitions are a significant component of the aurora and airglow in our atmosphere.

In the precise language of transition amplitudes, the probability that the electric field of a laser (or any light source) will stimulate an electric dipole transition between

[1] As with all explanations, this isn't the whole story. There are further selection rules for E1, E2 & M1 transitions which do not concern the 6P states of thallium. Furthermore, some of the rules given in the table make assumptions about LS coupling, among other things, and are therefore not "rigorous." See [Cor86].

two states $|\psi_a\rangle$ and $|\psi_b\rangle$ is proportional to

$$\left|\langle\psi_b|\ \vec{d}\cdot\vec{E}\ |\psi_a\rangle\right|^2. \tag{2.3}$$

For the $6P_{1/2}$ and $6P_{3/2}$ states, Expression 2.3 is identically zero when we make the E1 approximation that$\vec{E} = E_0\hat{\epsilon}e^{i\omega t}$ because the selection rules forbid it. Magnetic dipole interactions have an analogous expression for the amplitude of transitions between two states.

$$\left|\langle\psi_b|\ \vec{\mu}\cdot\vec{B}\ |\psi_a\rangle\right|^2. \tag{2.4}$$

Note that this operator is very different from the E1 operator, in that it acts only on angular momentum because $\vec{\mu} = \vec{L} + 2\vec{S}$. With a few calculations, we can compare the magnitudes of magnetic and electric dipole transitions. If we don't worry too much about numerical constants, $|\langle E1\rangle|^2 \propto (ea_0E)^2$ and $|\langle M1\rangle|^2 \propto (\mu_B B)^2$. The Bohr radius and Bohr magneton are defined in terms of more fundamental constants. In free space, Maxwell's equations tell us that $|B| = \frac{|E|}{c}$. Putting all of these together we find

$$\frac{\mathrm{M1}}{\mathrm{E1}} = \frac{1}{4}\left(\frac{e^2}{4\pi\epsilon_0\hbar c}\right)^2 = \frac{\alpha^2}{4} \tag{2.5}$$

Thus we learn that an M1 transition is approximately $\sim 10^4 - 10^5$ times *weaker* than an analogous E1 transition. The amplitude of E2 transitions is surprisingly similar to those of M1 transitions. Leo Tsai measured the ratio E2/M1 to be 0.239 in a measurement of optical polarization rotations in atomic thallium [Tsa98]. Needless to say, for our purposes there is nothing "forbidden" about the $6P_{1/2} \rightarrow 6P_{3/2}$ transition; if anything the experimental difficulties of measuring a weak transition help us by reducing the competition with other physicists.

2.3 Absorption Lineshapes

Our experiments take place in two different environments. The atomic beam unit and the vapor cell exhibit two different types of absorption lineshapes– gaussian and Voigt profiles– that deserve some discussion. In both cases, what we actually measure is the laser transmission through the sample:

$$T(\omega) = I_0 e^{-\delta(\omega)}, \tag{2.6}$$

where the incident light has an intensity I_0 and frequency ω. The function $\delta(\omega) = Nl\sigma(\omega)$ is the optical depth of the sample and is dependent on both the system configuration and atomic physics. The system parameters involved are atomic number density (N), which is itself dependent on temperature, and the distance over which the laser and atoms interacts (l). The relevant quantum mechanical entity is the absorption cross section ($\sigma(\omega)$), which is described below.

2.3.1 Voigt Profile

We use the vapor cell because it can provide much higher atomic densities and consequently greater optical depths, but measurements in the cell also have *much* greater linewidths than in the atomic beam, decreasing the precision of measurements. Even when we reduce the temperature so that the density is at the lowest limits of detectability, the linewidths are approximately 450MHz (FWHM), making it difficult to resolve the 500MHz spaced hyperfine transitions in each group and nearly impossible to resolve the isotope shift.

The primary reason for the broad absorption profile is that the laser beam must pass through the entire ensemble of atoms. The laser thus "sees" the complete Maxwell-Boltzmann distribution of atomic velocities. The absorption width (FWHM measured in frequency) of such a distribution is

$$\Delta = \frac{2\omega}{c}\sqrt{\frac{2k_B T \ln 2}{m}}, \tag{2.7}$$

where ω is the frequency of the light source, $2.3 \cdot 10^5$GHz (1283nm) in this case [Spe00][Dem98]. This works out to $\Delta = 11.51[\mathrm{MHz/K^{1/2}}]\sqrt{T}$ for thallium.

Atom-atom interactions are the secondary cause of broadening in the vapor cell. When two atoms approach each other their electron orbitals and energies shift; since each orbital is affected differently, the absorption frequencies change slightly. The effect is called "collisional broadening" or "pressure broadening" because the magnitude of the effect on the bulk gas increases as collisional rates (i.e. pressure) increase. When the effect is time averaged over the collection of atoms the net result is a lorentzian lineshape. If collisions were the only source of broadening, the cross section would be

$$\sigma(\omega) \propto \frac{\Gamma/2}{(\omega - \omega_0)^2 + \Gamma^2/4}, \tag{2.8}$$

where Γ is the FWHM and ω_0 is the natural absorption frequency. The parameter Γ is dependent upon pressure (P) and ultimately temperature, number density (N), collisional cross section (σ_c) and atomic mass (m) according to

$$\Gamma = 4\ P\sigma_c\sqrt{\frac{2}{\pi m k T}}. \tag{2.9}$$

In our vapor cell, thallium atoms are more likely to collide with helium atoms than with other thallium atoms, so Equation 2.9 is not strictly applicable. Over time, helium, which was used as a buffer gas, diffused into the cell when it was hot enough to become semipermeable. That residual helium now produces about 50 MHz of lorentz broadening. We plan to eliminate this residual collisional broadening in the near future with a new oven and cell that will be free of contaminants.

We must be careful in how we combine the collisional and Doppler broadening effects. Collisional broadening is a *homogenous* phenomenon in that all atoms have the same lorentz absorption lineshape. Doppler broadening, on the other hand is an

inhomogeneous ensemble effect. The Maxwell-Boltzmann distribution imparts a different, shifted absorption spectrum to each atom with a unique velocity. Therefore, when we calculate the cumulative effect we must use a convolution called a Voigt profile. One can think of this as an integration over the Maxwell-Boltzmann distribution, where, for each velocity, the atoms have a lorentz lineshape shifted by the appropriate Doppler factor.

$$\sigma(\omega) = A_0 \int_0^\infty \frac{\Gamma/2}{(\omega - \omega_0')^2 + \Gamma^2/4} \left(\frac{2}{\Delta\sqrt{\pi}}\right) e^{-\frac{4(\omega_0' - \omega_0)^2}{\Delta^2}} d\omega_0' \tag{2.10}$$

The coefficient A_0 is a quantum mechanical amplitude that determines the overall transition strength. It hardly needs to be said that this is an unwieldy expression. In the course of fitting the empirical lineshapes from the vapor cell measurement, we use a polynomial expansion of the integral. This approximation along with much more information about Voigt profiles are found in [Vet95].

It's worth noting that lifetime broadening is *not* a significant source of broadening in either the vapor cell or the atomic beam. This is because the $6P_{3/2}$ state is metastable. Since decay to the $6P_{1/2}$ ground state can only occur through improbable M1 and E2 transitions, the excited state is long lived. While there is certainly some finite lifetime broadening present in our measurements, it is below the level of detectability. Moreover, because lifetime broadening has the same form (lorentzian) as collisional broadening, this effect simply contributes to a slightly greater value for Γ in Equation 2.10.

2.3.2 Gaussian Lineshape

The atomic beam has a much simpler absorption cross-section. The atoms are created in a hot oven, much like the conditions in the vapor cell, but they are subsequently collimated so that only those travelling (nearly) perpendicular to the laser beam reach the interaction region. In the interaction region, the atomic density is sufficiently low that atomic collisions are unlikely. The remaining source of broadening is the small geometric divergence of the atomic beam in the plane of the probe laser. We can estimate the residual Doppler width with the general formula for Doppler shifts

$$\omega = \omega_0 \left(1 - \frac{v}{c}\right), \tag{2.11}$$

where ω_0 is the natural line center for an atom at rest and v is the velocity towards the laser source. In our apparatus the thallium oven is typically at a temperature of 800C, giving a mean velocity of 370m/s. The geometry of the collimators limit the divergence of the atoms to within 4^o of perpendicular to the laser propagation, barring some scattering. Thus we estimate that the Doppler width should be approximately $\Delta = \omega_0 \left(\frac{2 \cdot 370 m/s \sin 4^o}{c}\right) = 40$MHz. Charlie Doret's findings were consistent with this, once one accounts for the different values of ω_0 [Maj03]. The full expression for atomic

absorption cross-section is therefore

$$\sigma(\omega) = A_0 \left(\frac{2}{\Delta\sqrt{\pi}} \right) e^{-\frac{4(\omega-\omega_0)^2 \ln 2}{\Delta^2}}, \tag{2.12}$$

where, as before A_0, is a peak quantum mechanical transition strength. The constants $(\frac{2}{\Delta\sqrt{\pi}})$ are added so that the total cross-section, integrated over all frequencies remains constant as the Doppler width changes.

One idea for improving our apparatus involves reflecting the laser though the atomic beam multiple times, increasing l and σ. This multipass arrangement introduces some complications to the straightforward gaussian lineshape. Since the beams will follow slightly different paths through the interaction region, each pass will be at a slightly different angle to the beam, so the final absorption lineshape will be a sum of shifted gaussians. For reasons established in Appendix B, the departure from a pure gaussian will be small, assuming the maximum deviation of the laser from perpendicular is less than 5ºand that we have more than 3 passes. Consequently our fitting routines do not need modification.

2.3.3 Quantum Mechanical Amplitudes

The quantity A_0 that appears in both Equations 2.10 and 2.12 deserves some discussion. These quantum mechanical amplitudes determine the magnitude of the absorption and are derived from the transition matrix elements that "connect" the initial and final states under consideration. Consequently, A_0 is unique to each pair of initial and final states. For the transitions that we study, the total amplitudes are a combination of M1 and E2 components depending on the transition.[2] When in an electric field, there is also an additional Stark induced E1 amplitude. The magnetic dipole amplitudes are particularly easy to calculate from theory because the dominant terms are spin-dependent. In contrast, the E2 and Stark induced amplitudes come from spatial integrals of wavefunctions and the transition operator, which are notoriously difficult to derive from theory. Therefore the quantity E2/M1 (or Stark-E1/M1) provides a direct test of wavefunction accuracy. We measure these ratios rather than E2 (or Stark-E1) amplitude directly because the actual absorptivities that we can measure in the laboratory depend on atomic density as well as intrinsic quantum mechanical strength; the ratio is independent of the unknown atomic density.

2.4 Stark Shift

The Stark shift is a well known quantum mechanical phenomenon that arises when one puts atoms in an external static electric field. The electric field perturbs the

[2]There are also negligible contributions to A_0 from higher order multipole transitions and PNC-E1.

Hamiltonian of the system and introduces corrections to the energies of all states. There is no first order correction because such a term would be

$$\mathcal{E}_n^{(1)} = eE\langle\psi_n^0|z|\psi_n^0\rangle \tag{2.13}$$

and clearly $|\psi_n\rangle$ and $z|\psi_n\rangle$ have opposite parity. Even though there are degenerate m_F states in thallium, we can use non-degenerate perturbation theory, because the integral represented by Equation 2.13 is a *spatial* one and there are *no* degenerate spatial wavefunctions. Thus $\mathcal{E}_n^{(1)} = 0$ and there is no linear Stark shift in thallium. We now consider second-order corrections to the energies of states.

$$\mathcal{E}_n^{(2)} = \sum_{m\neq n} \frac{\left|\langle\psi_m^0|H'|\psi_n^0\rangle\right|^2}{\mathcal{E}_n^{(0)} - \mathcal{E}_m^{(0)}} = |E|^2 \sum_{m\neq n} \frac{\left|\langle\psi_m^0|ez|\psi_n^0\rangle\right|^2}{\mathcal{E}_n^{(0)} - \mathcal{E}_m^{(0)}}, \tag{2.14}$$

is the energy correction for state n, where $H' = \vec{d}\cdot\vec{E} = -eEz$ is the perturbation due to the field $\vec{E} = E\hat{z}$ and $\vec{d} = e\vec{r}$ is the dipole operator. The outcome of this calculation is that the energy level of each state shifts in proportion to the electric field squared (the quadratic Stark shift). In shorthand,

$$\Delta\mathcal{E}_n = \beta_n E^2, \tag{2.15}$$

where β_n incorporates all the information about wavefunctions contained in the sum in Equation 2.14. In practical laboratory terms, what we can measure is the difference in energies between two energy levels. Thus what we actually observe is

$$\begin{aligned} \Delta\omega &= \tfrac{\Delta\mathcal{E}_i - \Delta\mathcal{E}_f}{h} \\ &= \tfrac{\beta_i - \beta_f}{h} E^2 \\ &= k_{Stark} E^2 \end{aligned} \tag{2.16}$$

where

$$k_{Stark} = \frac{\beta_i - \beta_f}{h}. \tag{2.17}$$

Because k_{Stark} is closely related to the sums over wavefunctions and is directly measurable in the laboratory, it provides a convenient avenue for atomic structure checks on electroweak effects.

Doret obtained a value of -103.34(39)kHz/(kV/cm)^2 for $k_{Stark}^{(378nm)}$. A quick appraisal of $\mathcal{E}_n^{(2)}$ can give us an idea of the relative size of $k_{Stark}^{(1283nm)}$. For the ground state, $6P_{1/2}$, all Stark mixing will occur with higher energy states, so the ground state will shift downward in energy, as usual. The $6P_{3/2}$state can't mix with states of the same parity, so it also mixes only with higher energy states. Moreover, because the $6P_{3/2}$state is closer in energy to $7S_{1/2}$ than is the $6P_{1/2}$state, it should have a greater negative shift than the ground state. The $7S_{1/2}$ state used in Doret's work mixes with states of both higher and lower energy, but the closed mixed state ($7P_{1/2}$) is just slightly higher in energy, making the downward shift of $7S_{1/2}$ quite large. As a result, we expect $k_{Stark}^{(1283nm)}$ to be smaller in magnitude than $k_{Stark}^{(378nm)}$, but still negative.

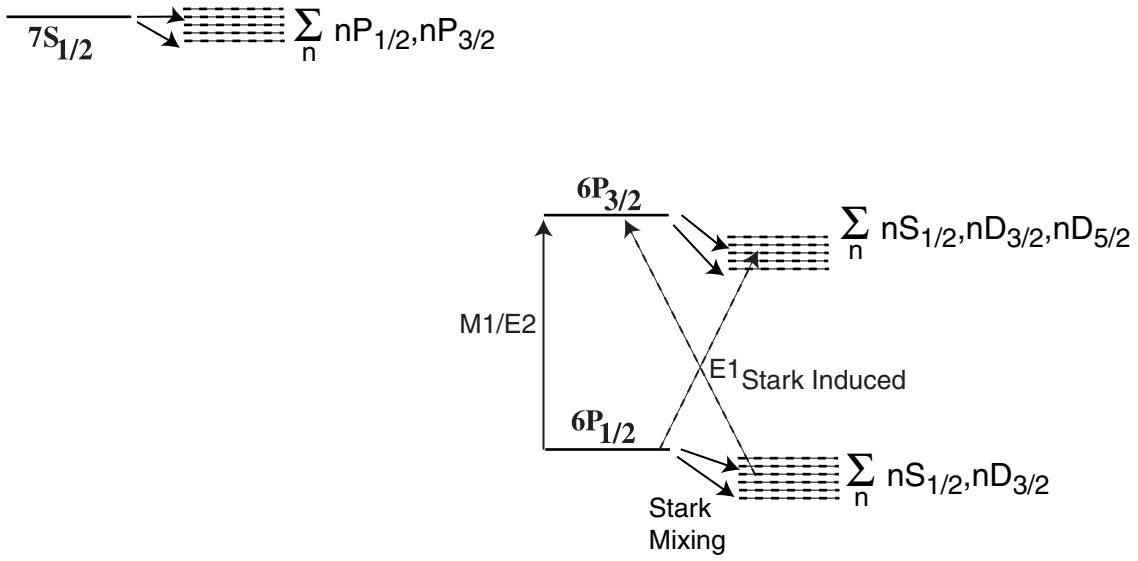

Figure 2.3: Unperturbed (solid) and Stark mixed (dashed) states and transitions.

2.4.1 Stark Induced Amplitudes

In the presence of an electric field, the amplitudes of M1 and E2 transitions, such as we study, change dramatically. This occurs because the external field mixes the 6P states with other states of opposite parity. (See Figure 2.3.) Thus the states that we are studying obtain some character of the $7S_{1/2}$ state. In principle, all S and D states contribute to the sum in Equation 2.14, but since the other S and D states are farther away in energy, they make a smaller contribution. With the presence of the $7S_{1/2}$ state, E1 transitions to the $6P_{3/2}$ states become possible. Because E1 transitions occur with much greater amplitude than M1 and E2 transitions, the small E1 component is significant compared with the unperturbed transition amplitude. Measurements of the induced amplitudes, like the measurements of the shift itself provide a measure of the mixing between unperturbed states and therefore a check on the accuracy of theoretical wavefunctions. I expect those reading this are probably familiar with Charlie Doret's measurement of k_{Stark} for the $6P_{1/2} \rightarrow 7S_{1/2}$ transition and might wonder why his data do not exhibit induced amplitudes. The reason is that, to second-order, the states mixed into the $6P_{1/2}$ state are S and D states. The additional transitions to $7S_{1/2}$ allowed by this mixing are all weak M1 and E2 transitions, so the (already large) E1 amplitude does not change appreciably.

The following equation puts some flesh on the processes depicted in Figure 2.3. The Stark amplitude contributes to the A_0's that appear in Equations 2.10 and 2.12. Since the static field opens up two new E1 pathways for the $6P_{1/2} \rightarrow 6P_{3/2}$ transition, there are two corresponding terms in the expression for the Stark induced amplitude ([DBC94]). Note that each summation represents a two step process: mixing either the initial or final state via the static electric field ($\vec{E}$) and a transition stimulated by

the laser ($\vec{\epsilon}$).

$$A_{Stark} = \sum_{m \neq 6P_{3/2}} \frac{\langle 6P_{3/2}|\vec{E}\cdot\vec{d}|m\rangle\langle m|\vec{\epsilon}\cdot\vec{d}|6P_{1/2}\rangle}{\mathcal{E}^{(0)}_{6P_{3/2}} - \mathcal{E}^{(0)}_{m}} + \sum_{m \neq 6P_{1/2}} \frac{\langle 6P_{1/2}|\vec{E}\cdot\vec{d}|m\rangle\langle m|\vec{\epsilon}\cdot\vec{d}|6P_{3/2}\rangle}{\mathcal{E}^{(0)}_{6P_{1/2}} - \mathcal{E}^{(0)}_{m}} \quad (2.18)$$

The structure of this equation tells us that the Stark induced amplitudes will be slightly different depending on the relative orientations of the laser polarization and the static electric field. From the point of view of testing physical theory, this equation is interesting because, like Equation 2.16, it is a directly measurable quantity (i.e. turn $\vec{E}$ on and off and watch A change) that requires accurate knowledge of many wavefunctions to predict. The induced amplitude involves a different sum than Equation 2.16, so each effect provides a unique check on theoretical accuracy.

Throughout this chapter, the weak interaction has been lurking in the shadows. While we do not measure the effects of this electron-nucleon interaction in this experiment, the fact that it exists motivates this work. In some ways it acts like the Stark effect in that it mixes the 6P states with states of the opposite parity, modifying their energies and inducing a small E1 component in the 1283nm transition, but I must emphasize that this is effect is there regardless of the presence of an electric field or any other externally adjustable parameter, so its presence is indistinguishable from the background M1 and E2 transitions and undetectable in this work.

Chapter 3

Frequency Modulation

Frumpety-Lumpety
Gallagher's laser group
improved their signal/noise
ratio, *sooo...*

we use their method (it's
"two-tone spectroscopy"),
helping us see things where
O.D. is low.

A variation on frequency modulation (FM) is at the heart of our detection technique. Therefore, understanding the mathematical foundations of FM is central to this experiment. Because FM may be unfamiliar to the reader, I will give a summary of the mathematical derivations commonly used with FM signals before explaining what "two-tone" modulation is and how it is helpful.

3.1 AM Refresher

The important features of FM are more apparent when compared with amplitude modulation (AM), so I will briefly review how one derives the frequency spectrum of a single tone AM modulation. If the carrier's electric field is described by $E(t) = E_0 \sin(\omega_c t)$, then the AM electric field is traditionally given by $E_{AM}(t) = E_0(1 + B\cos(\omega_m t))\sin(\omega_c t)$. Using basic trigonometric identities, one can reexpress this product as a sum containing the sines of the sum and difference frequencies:

$$E_{AM}(t) = E_0 \sin(\omega_c t) + E_0 B/2[\sin(\omega_c - \omega_m)t + \sin(\omega_c + \omega_m)t]. \tag{3.1}$$

Note that there are three frequency components, all of which have the same phase (all are positive sine functions). (See Figure 3.1.)

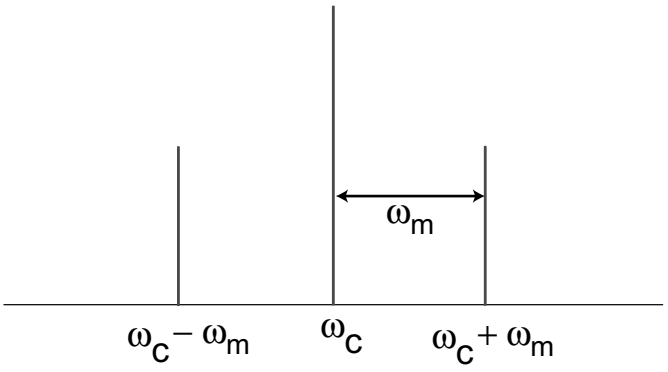

Figure 3.1: AM electric field spectrum for B=1.

3.2 FM Basics

Now we are ready to take the big step into the FM world. Let's revisit the equation for the carrier wave: $E(t) = E_0 \sin(\omega_c t + \phi)$. Note that now I have included a phase term. We could have used it above when we discussed AM, but through choice of origin, we could eliminate it. However the phase becomes essential in FM. This time we will leave E_0 constant, but allow ϕ to vary. In the simplest case, ϕ could be a sine wave: $\phi(t) = \beta \sin(\omega_m t)$.[1] The parameter β is known as the modulation index, or modulation depth because it controls the "strength" of the modulation similar to the way that B determines the "strength" of AM.[2] Other references may use m or $\Delta\omega_{peak}/\omega_m$ instead of β. I shall use β because it seems to be more common in the spectroscopy literature. The full expression for the electric field is $E(t) = E_0 \sin(\omega_c t + \beta \sin(\omega_m t))$, a concise but unhelpful expression. At this point in the derivation, some texts distinguish between narrowband FM, where $\beta \ll \pi$, and wideband FM, where $\beta \gtrsim \pi$. The narrowband case is much simpler because the carrier and first order sidebands dominate the frequency spectrum in this regime, whereas higher order sidebands become significant in the wideband case. I shall use the general (wideband) equations equations because our system exists in this regime.

[1] If one is being very careful with terminology, what I have described is phase modulation. True frequency modulation leaves ϕ constant and replaces $\omega_c t$ in the above equations with $\int \omega(t)dt = \int(\omega_c + \Delta\omega_{peak} \cos(\omega_m t))dt$ so that it really is the frequency that varies. Integrating this expression gives $\int \omega(t)dt = \omega_c t + \frac{\Delta\omega_{peak}}{\omega_m} \sin(\omega_m t) + \phi_0$, which differs from the case in the text by only a constant, hence inconsequential, phase difference. Thus phase modulation and true frequency modulation are generally both referred to as FM.

[2] There is no FM analog to 100% amplitude modulation. While the AM spectrum changes dramatically when $B \geq 1$, β can be as large as one desires or is able to produce without qualitatively changing the spectrum.

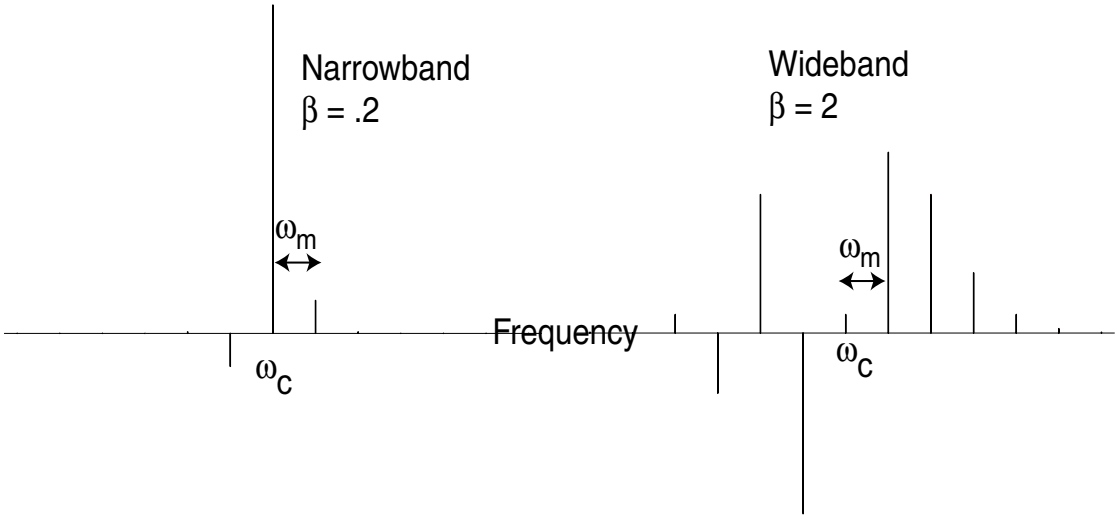

Figure 3.2: Two FM E-field spectra with the same total power and different β's.

We continue the frequency spectrum derivation by using a trig identity

$$E(t) = E_0 \sin(\omega_c t + \beta \sin(\omega_m t)) = E_0 \left[\sin \omega_c t \cos(\beta \sin \omega_m t) + \cos \omega_c t \sin(\beta \sin \omega_m t)\right]. \tag{3.2}$$

At this point, one needs either divine inspiration or a very extensive volume of series expansions. The appropriate choice is the Jacobi-Anger Expansion. Without further delay let's apply it:

$$\begin{aligned} E(t) &= E_0 \sin \omega_c t \left[J_0(\beta) + 2 \sum_{n>0,\ even}^{\infty} J_n(\beta) \cos(n\omega_m t) \right] \\ &\quad + E_0 \cos \omega_c t \left[2 \sum_{n>0,\ odd}^{\infty} J_n(\beta) \sin(n\omega_m t) \right] \end{aligned} \tag{3.3}$$

With a few more strategic applications of trigonometric identities, we can find the frequency spectrum:

$$\begin{aligned} E(t)/E_0 = \ & J_0(\beta) \sin \omega_c t \\ & + J_1(\beta) \left[\sin(\omega_c + \omega_m)t - \sin(\omega_c - \omega_m)t\right] \\ & + J_2(\beta) \left[\sin(\omega_c + 2\omega_m)t + \sin(\omega_c - 2\omega_m)t\right] \\ & + J_3(\beta) \left[\sin(\omega_c + 3\omega_m)t - \sin(\omega_c - 3\omega_m)t\right] \\ & + \ldots \end{aligned} \tag{3.4}$$

Figure 3.2 shows this electric field spectrum for both narrowband and wideband cases.

3.3 FM Spectroscopy

Narrowband FM spectroscopy is a well-established technique for improving the sensitivity of an experiment. This spectroscopic technique requires that ω_c be tunable

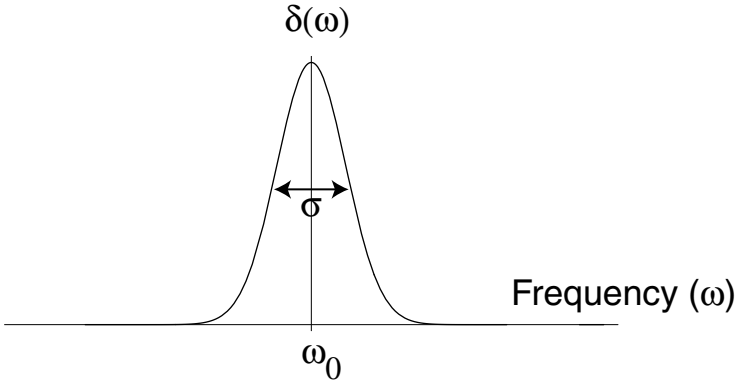

Figure 3.3: Gaussian absorption profile.

across the absorption frequencies. If ω_m is greater than the width of the absorption, then the results are generally easier to interpret, but so long as ω_m is not negligible compared with the FWHM, the technique will work. In an experimental implementation, ω_c is typically a visible or near-visible light transition and ω_m is in the radio regime. The FM wave is transmitted through the absorbing medium and the intensity of the emerging wave is demodulated at ω_m, either with a lock-in amplifier or heterodyne detection. This works because noise can enter the final measurement only if it is near the detection frequency ω_m, and typically noise decreases for higher (i.e. radio) frequencies.

We can do an analytic approximation of the demodulated signal for narrowband FM. Let's assume that the absorption feature we want to study, whatever it's source, has a gaussian profile. (Figure 3.3, σ is the FWHM)

$$\delta(\omega) = \delta_0 \exp\left[-\left(\frac{\omega-\omega_0}{\sigma}\right)^2 \ln 2\right] \tag{3.5}$$

The corresponding transmission of a wave with frequency ω through the absorbing medium is $\exp(-\delta(\omega))$; however, rather than writing this exponential repeatedly, we use the shorthand $T(\omega)$ to indicate the transmission. Each of the frequency components of the FM wave will be absorbed differently. After passing through the interaction region the electric field is:

$$\begin{aligned} E'(t) &= E_0[T(\omega_c)J_0(\beta)\sin\omega_c t \\ &\quad - T(\omega_c-\omega_m)J_1(\beta)\sin(\omega_c-\omega_m)t \\ &\quad + T(\omega_c+\omega_m)J_1(\beta)\sin(\omega_c+\omega_m)t] \end{aligned} \tag{3.6}$$

For the moment we can ignore the higher order terms because $J_n(\beta)$ decreases rapidly as n increases, assuming β is small, as we have since we are only dealing with narrowband FM.

The detector, regardless of its type, "sees" intensity rather than electric field, so the detected signal is:

$$I(t) = \langle c\epsilon_0 E'^2(t) \rangle \tag{3.7}$$

We must carefully specify what we mean by a time average in this case. No detector is fast enough to detect the beats of an optical carrier wave, so we must average over ω_c; however there are photodiodes that work at radio frequencies (and this is exactly what we need to make this work), so we should *not* average over ω_m. The derivation is tedious, but requires only simple trigonometric identities, so I will forgo writing it here and skip directly to the (more interesting) result:

$$\begin{aligned} I(t) &= \frac{c\epsilon_0 E_0^2}{2}[\exp(-2A(\omega_c))J_0^2(\beta) \\ &\quad + T^2(\omega_c - \omega_m)J_1^2(\beta) \\ &\quad + T^2(\omega_c + \omega_m)J_1^2(\beta) \\ &\quad + T^2(\omega_c)T^2(\omega_c + \omega_m)J_0(\beta)J_1(\beta)\cos\omega_m t \\ &\quad - T^2(\omega_c)T^2(\omega_c - \omega_m)J_0(\beta)J_1(\beta)\cos\omega_m t \\ &\quad - T^2(\omega_c - \omega_m)T^2(\omega_c + \omega_m)J_1^2(\beta)\cos 2\omega_m t] \end{aligned} \tag{3.8}$$

With heterodyne or lock-in detection, we can select just the intensity component with frequency ω_m. The demodulated intensity is then:

$$\begin{aligned} I_{demod}/E_0^2 &= T^2(\omega_c)T^2(\omega_c + \omega_m)J_0(\beta)J_1(\beta) \\ &\quad - T^2(\omega_c)T^2(\omega_c - \omega_m)J_0(\beta)J_1(\beta) \end{aligned} \tag{3.9}$$

The demodulated absorption signal depends on the *difference* in transmission at frequencies $\omega_c+\omega_m$ and $\omega_c-\omega_m$. The plot in Figure 3.4 shows the demodulated output as the carrier frequency is swept through the resonance centered at ω_0. Notice that the signal is zero when the carrier is absorbed, but nonzero when either of the sidebands is absorbed.

Do I hear you thinking, "Why would anyone do something like this?" After all, RF equipment, modulators and demodulators just make things more complicated, not to mention more expensive. Here's why: the detection frequency is now ω_m, compared with DC for standard transmission spectroscopy. Almost all noise diminishes as frequency increases, so the signal to noise ratio is potentially much higher. With that in mind, it seems best to go to very high frequencies; however, there are practical limitations on how large ω_m can be. Photodetectors and electronics for modulation and demodulation get progressively more expensive as one moves to higher radio frequencies. At the far reaches of the radio spectrum, coaxial cables become inefficient waveguides, so even laboratory materials must change.

3.4 Two-Tone Modulation

Some clever folks at the University of Virginia devised a modification of FM spectroscopy that maintains the signal to noise advantages of high frequencies, while low-

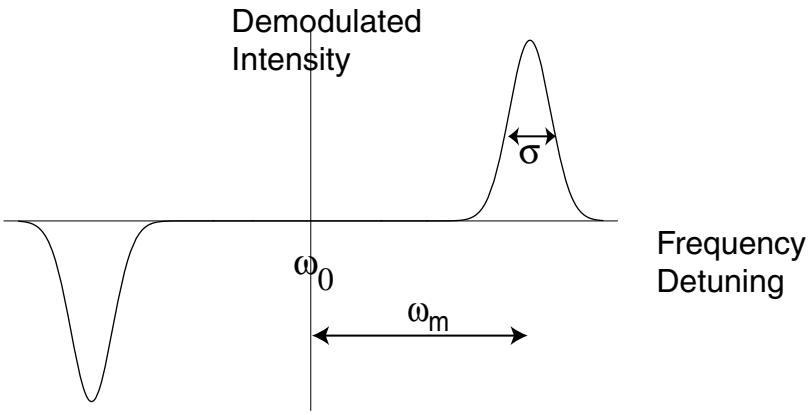

Figure 3.4: FM spectroscopy signal.

ering the detection frequency to reside more comfortably within the range of easily available electronics. If you haven't guessed already, this is called "two-tone modulation." The additional mathematical complication is that we modulate the carrier at *two* frequencies (i.e. $\omega_m + \Omega/2$ and $\omega_m - \Omega/2$) that differ by a small amount $\Omega \ll \omega_m$, and later demodulated at the difference frequency Ω. At this point it becomes much easier to adopt the complex phasor notation for an electric field. If the unmodulated carrier is $\tilde{E}_0 e^{i\omega_c t}$, then a single FM modulation is

$$\tilde{E}(t) = \tilde{E}_0 e^{i(\omega_c t + \beta \sin(\omega_m t))}. \tag{3.10}$$

A different form of the Jacobi-Anger Expansion will give us the frequency spectrum in complex representation:

$$\tilde{E}(t) = \tilde{E}_0 e^{i(\omega_c t + \beta \sin(\omega_m t))} = \tilde{E}_0 e^{i\omega_c t} \sum_{n=-\infty}^{\infty} J_n(\beta) \exp(in\omega_m) \tag{3.11}$$

With two modulation frequencies the expression lengthens:

$$\begin{aligned} \tilde{E}(t) &= \tilde{E}_0 e^{i(\omega_c t + \beta_- \sin(\omega_m - \Omega/2)t + \beta_+ \sin(\omega_m + \Omega/2)t)} \\ &= \tilde{E}_0 e^{i\omega_c t} \left[\sum_{n=-\infty}^{\infty} J_n(\beta_-) \exp[in(\omega_m - \Omega/2)t] \right] \\ &\quad \left[\sum_{n=-\infty}^{\infty} J_n(\beta_+) \exp[in(\omega_m + \Omega/2)t] \right] \end{aligned} \tag{3.12}$$

This unwieldy expression simplifies dramatically if $\beta_+ = \beta_- = \beta$ and if we are in the narrowband regime where $\beta \ll \pi$. In what follows, I will use an analytic form for the narrowband limit. Although our apparatus lies slightly outside this range the narrowband equations provide a good insight into what really happens. See Appendix A for a description of our simulation of the full (wideband) two-tone case. Here we

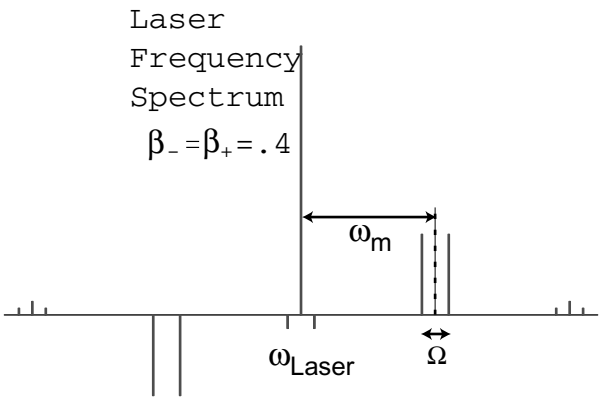

Figure 3.5: Two-tone modulation spectrum

ignore all terms of the sum except $n = 0$ and $n = \pm 1$. In this limit, one could also make the approximations that $J_0(\beta) = 1$ and $J_1(\beta) = \beta/2$, but I won't do this so as to preserve a more accurate functional form. Together these substitutions produce:

$$\begin{aligned}\tilde{E}(t) &= \tilde{E}_0[J_0^2(\beta)\exp(i\omega_c t) - J_1^2(\beta)\exp[i(\omega_c+\Omega)t] - J_1^2(\beta)\exp[i(\omega_c-\Omega)t] \\ &\quad - J_0(\beta)J_1(\beta)\exp[i(\omega_c-\omega_m-\Omega/2)t] - J_0(\beta)J_1(\beta)\exp[i(\omega_c-\omega_m+\Omega/2)t] \\ &\quad + J_0(\beta)J_1(\beta)\exp[i(\omega_c+\omega_m-\Omega/2)t] + J_0(\beta)J_1(\beta)\exp[i(\omega_c+\omega_m+\Omega/2)t]\end{aligned} \tag{3.13}$$

The significant features of this spectrum are conveyed in Figure 3.5. Each sideband now has two components, with the same phase as their counterparts in the single tone FM spectrum. In addition, there are two small components very close to the carrier. These are intermodulation products that are present due to interference between the two modulating frequencies.

We model absorption in almost the same way as we did for single-tone FM. As before, the carrier and upper and lower sidebands each have their own characteristic absorption. A judicious choice of Ω will make the signal much easier to interpret. If Ω is much smaller than the width of the absorption, then we can say that the absorption of the $\omega_c + \omega_m + \Omega/2$ and $\omega_c + \omega_m - \Omega/2$ frequencies are the same, and similarly for the lower sideband group. Thus there are really only three distinct transmission coefficients. The last steps to obtaining the demodulated intensity are the same as in Section 3.3, but because of the greater number of terms to multiply, the calculation requires greater fortitude or Mathematica. (Recall $I = \frac{\epsilon_0 c}{2}\mathrm{Re}(\tilde{E}(t)\tilde{E}^*(t))$ The result one hopes to obtain after selecting only terms at freuqncy Ω is:

$$I_{demod} = 4c\epsilon_0|\tilde{E}_0|^2[J_0(\beta)J_1(\beta)]^2\left[T^2(\omega_c-\omega_m) + T^2(\omega_c+\omega_m) - 2T^2(\omega_c)\right] \tag{3.14}$$

Figure 3.6 shows a scan through a gaussian absorption using this modulation technique. Like the standard FM spectroscopy, the signal is zero, except when one of the sidebands or the carrier is absorbed. The amplitude of the central peak is twice the

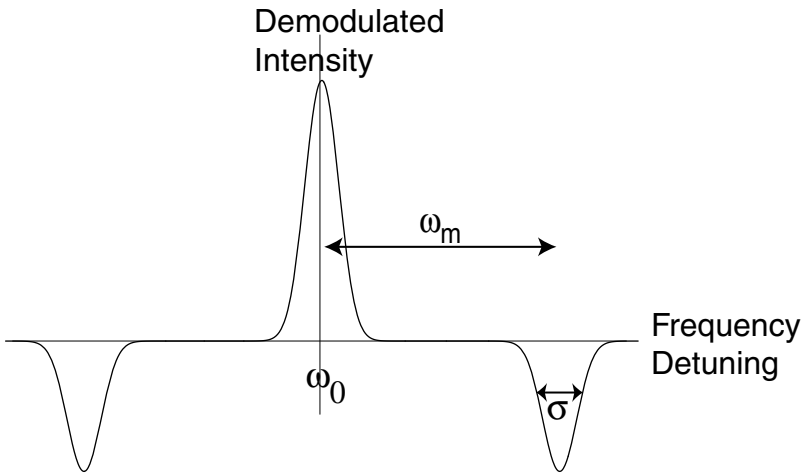

Figure 3.6: Demodulated two-tone signal.

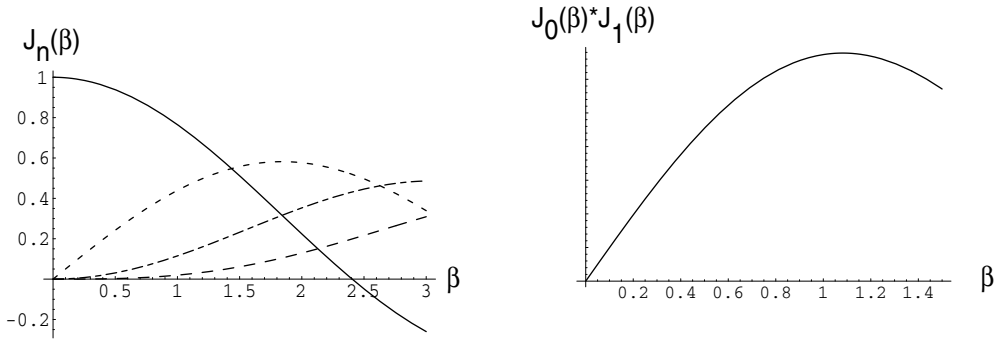

Figure 3.7: Bessel functions 1-4; Product of J_0 and J_1.

others; but all of them scale together with the quantity $[J_0(\beta)J_1(\beta)]^2$, so we would like to maximize this quantity in our apparatus. We find from plotting Bessel functions and their product, that the signal should be maximum when $\beta = 1.08$. (See Figure 3.7.) As with FM spectroscopy, in two-tone spectroscopy ω_c is typically in the optical range and ω_m in the RF, but now Ω can be much lower, where electronics are more readily available and much cheaper.

3.5 Residual Amplitude Modulation

As with any experiment, we seek to reduce the sources of noise and background signals in our apparatus. One of the most significant that we have faced is residual amplitude modulation (RAM). The RAM is pernicious when it occurs at the same frequencies as the desirable FM, because it can easily be much larger than the signals we hope to observe. (In fact, we don't care if it exists at other frequencies because our lock-in amplifier has a narrow detection bandwidth.)

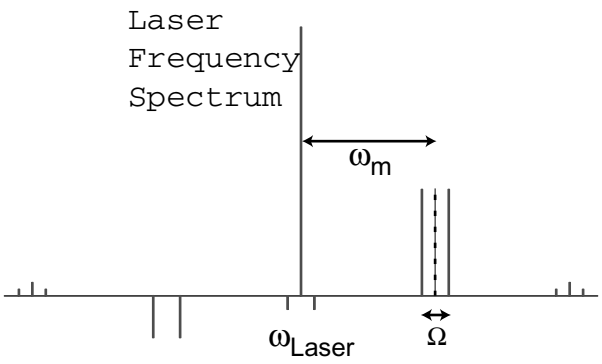

Figure 3.8: Two-tone spectrum with RAM: $\beta = .4, A_{RAM} = .15$

The frequency spectrum of a carrier modulated with both AM and FM is simply the sum of frequency spectra for each modulation individually. Therefore if we have RAM with amplitude A_{RAM} at both of the two-tone frequencies, the complete electric field spectrum is:

$$\begin{aligned}\tilde{E}(t) &= \tilde{E}_0[J_0^2(\beta)\exp(i\omega_c t) - J_1^2(\beta)\exp[i(\omega_c+\Omega)t] - J_1^2(\beta)\exp[i(\omega_c-\Omega)t] \\ &\quad - (J_0(\beta)J_1(\beta) - A_{RAM})\exp[i(\omega_c-\omega_m-\Omega/2)t] \\ &\quad - (J_0(\beta)J_1(\beta) - A_{RAM})\exp[i(\omega_c-\omega_m+\Omega/2)t] \\ &\quad + (J_0(\beta)J_1(\beta) + A_{RAM})\exp[i(\omega_c+\omega_m-\Omega/2)t] \\ &\quad + (J_0(\beta)J_1(\beta) + A_{RAM})\exp[i(\omega_c+\omega_m+\Omega/2)t]] \end{aligned} \tag{3.15}$$

Here we use the narrowband FM approximation. Also note that, as always, AM leaves the carrier amplitude unchanged but introduces a pair of symmetric sidebands separated from the carrier by the modulation frequency. The effect of the RAM is readily apparent in Figure 3.8, which shows the frequency spectrum with RAM. Note that the sidebands are no longer antisymmetric and that the effect is analogous to a pure two-tone spectrum constant background absorption of the lower sideband pair.

I'll forgo the derivation of the demodulated intensity (again, demodulated at the difference frequency Ω) and simply state the result. Furthermore, we use the additional shorthand T_0, T_{+1}, T_{-1} to refer to the transmission amplitudes of the carrier, upper and lower sidebands respectively.

$$\begin{aligned}I_{demod} &= 4c\epsilon_0|\tilde{E}_0|^2 \quad [J_0^2(\beta)J_1^2(\beta)(T_+^2 + T_-^2 - 2T_0^2) \\ &\qquad + A_{RAM}^2(T_+^2 + T_-^2) + J_0(\beta)J_1(\beta)A_{RAM}(T_+^2 - T_-^2)] \end{aligned} \tag{3.16}$$

This expression is the same as the pure two-tone case (Equation 3.14) with several additional terms. The A_{RAM}^2 term produces a constant offset away from any absorption features Meanwhile the $J_0(\beta)J_1(\beta)A_{RAM}$ term gives the demodulated spectrum

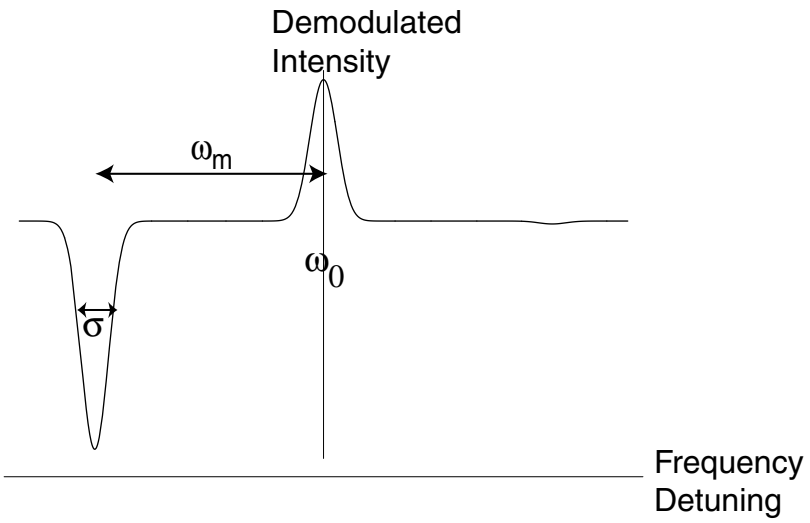

Figure 3.9: Demodulated two-tone signal with RAM. ($\beta = .4, A_{RAM} = .15$)

an asymmetry. Figure 3.9 shows the effect that RAM has on the demodulated signal. Note the asymmetry and offset are large despite the fact that $A_{RAM} < \beta$.

The causes of RAM are an ongoing subject of debate. Some sources, such as etalons have been known for some time, but others sources are still unknown. An etalon produces RAM when one of the sidebands of the spectrum has a higher transmission through the resonant cavity than do the others. This occurs when one sideband frequency is very near the cavity resonance while the others are far away. The asymmetry passively produced in this manner is equivalent to active amplitude modulation in its effects. We attempt to reduce this by slightly "misaligning" some optics, such as the EOM, and the vacuum chamber windows. Another source of RAM is the EOM. A poor quality crystal can produce excessive RAM, but if that is the case, there is nothing that the user can do short of sending the item back to the manufacturer. At present we see 10μV of RAM. This is no problem when looking for a signal in the vapor cell, where signals of 1V are possible. We expect that the magnitude of the signal in the atomic beam will be on the order of 10μV, so are considering different ways of eliminating this background. Our upgrades to the chopping wheel for the atomic beam may help with RAM. Even without fixing any problems, the DC offset on the lock-in output is a simple way to make small RAM offsets invisible to the data collection software.

Chapter 4

The Apparatus

Snap-Oops-Splat, Whiz-Pop-Bang,
Tiku Majumder's lab
labors to measure all
thallium's specs.

Using equipment with
ideosyncracies,
one always hopes to find
what one expects.

We can easily divide our laboratory apparatus into three parts according to production roles. The three things we do are: produce laser light, produce atoms, and process the signals.

4.1 Optics

The optical system is a realization of the two-tone modulation scheme discussed in Chapter 3. The schematic in Figure 4.1 shows briefly how we produce laser light with the proper sideband structure. In this section, I discuss how each component contributes to creating the modulated laser light.

4.1.1 The Diode Laser

The present work uses a 1283nm external cavity diode laser from Sacher Lasertechnik. The Littrow configuration (see Figure 4.2 for a schematic and [Fri01] for more information) gives us substantial power output (12mW) and mode hop-free tunability over a wide frequency range. As with all diode lasers, the power and frequency output of the Sacher laser are affected by temperature, grating position and diode current. This is both a boon and a burden because it gives us flexibilty to reach a great range of wavelengths, but also introduces many potential sources of error that we must minimize.

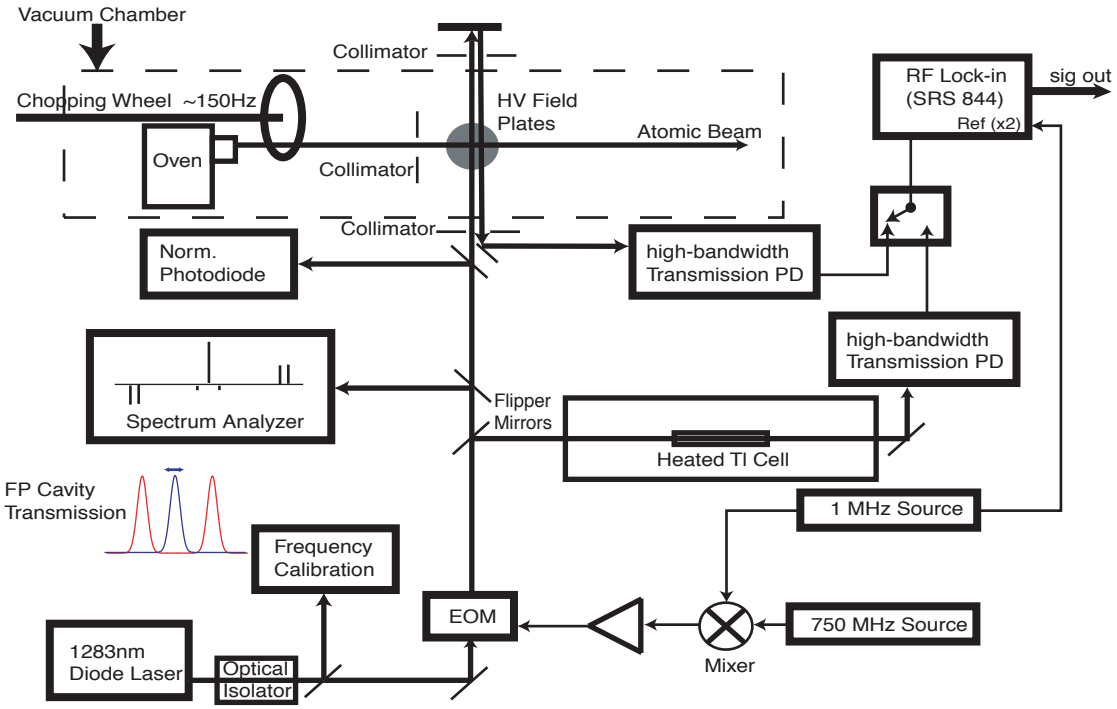

Figure 4.1: The Optical System

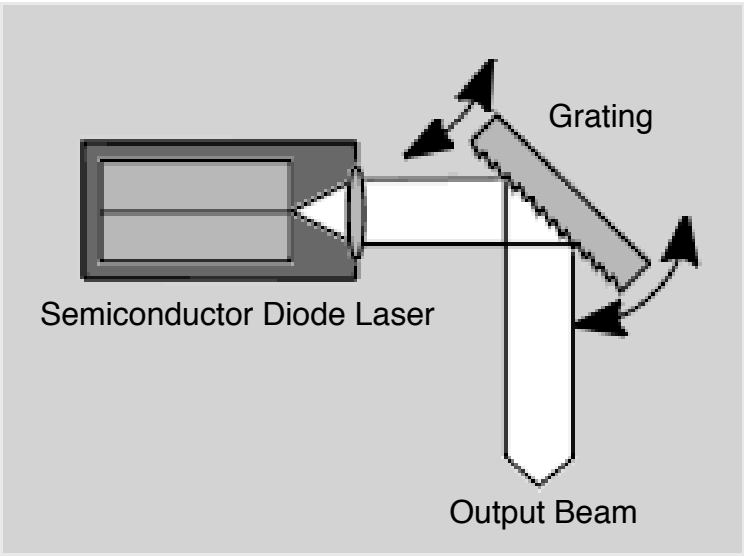

Figure 4.2: Littrow Laser Design (from [Fri01])

We spent some time exploring what operating conditions are best for reaching the precise wavelengths of the 1283nm thallium transition, simultaneously optimizing the output power. In general the diode should be slightly below room temperature, in the vicinity of 15°C. One should not further reduce the temperature because condensation may form in the unit. Having found that a diode current of ∼50mA produces ample and stable power output we rarely adjust this parameter.

The grating position deserves some further discussion. Adjusting the voltage to the piezo-electric transducer (PZT, for good reason!) that controls the grating position is the primary and easiest means of changing the laser frequency. However, one must not fall into the trap of using the high voltage PZT driver provided by Sacher, as this has an unsatisfactory amount of jitter in the voltage. Paul Friedberg constructed a much more stable variable source which we use instead ([Fri01]). With this device the laser frequency is constant to within 1-2MHz over a period of many seconds, in contrast with tens of megahertz noise using the Sacher driver.[1] The homemade device has a bias input that allows one to make small frequency sweeps, via either a computer or a function generator input ([Fri01]). We minimize long term frequency drifts by enclosing the laser in an acrylic box containing acoustic foam. Long-term drifts remain, but these should not be a problem for our experiments because collecting data is fast relative to the drift speed. Many drifts can are also monitored with the Fabry-Perot cavity described below so that we can correct for them in the final data analysis. If adjustments to temperature, diode current and PZT voltage are not enough to reach the desired wavelength, one can open the casing and manually move the grating until satisfied.

Diode lasers are notoriously sensitive to retroreflections from downstream optics. Such feedback can cause the laser's power and frequency output to behave erratically. The danger is especially great if there are high-Q devices, such as Fabry-Perot cavities or highly-reflective optics, in the beam path. With a 40dB optical isolator, we have not noticed any trouble with reflection instabilities.

4.1.2 Fabry-Perot Cavity

In the course of scanning the laser through an atomic absorption, the parameter that we actually control and vary is the bias voltage to the PZT. All physically interesting phenomena are dependent on the laser's frequency, so we need to convert voltage into frequency. Ideally the frequency would vary linearly with voltage, but it will be no surprise to an experimentalist that there are non-linearities and hysteresis in the PZT response that we should consider. Figure 4.3 shows a realistic plot of optical frequency versus input voltage, making it clear why we need an independent calibration source. The Fabry-Perot etalon helps us circumvent the nonlinearities. Some of the laser light is picked off immediately following the optical isolator and sent into the etalon. As we

[1] We measure this noise against a stabilized He-Ne laser using the scanning Fabry-Perot cavity previously used to frequency-lock the diode. See [Spe00] for operational details. For the present work the same etalon is used in a passive manner described in Section 4.1.2, but can easily be switched between active and passive modes of operation.

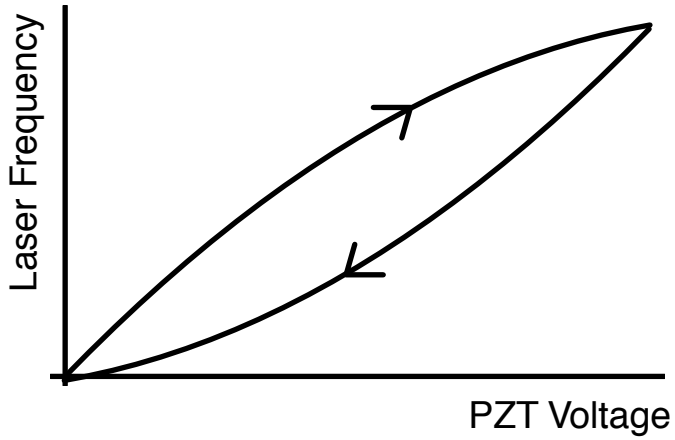

Figure 4.3: Non-linear frequency response and hysteresis of laser PZT (simulated)

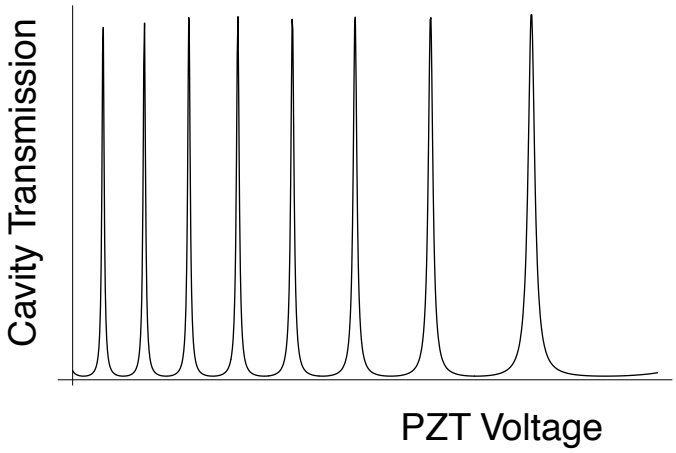

Figure 4.4: Effect of nonlinear PZT on FP transmission (simulation greatly exaggerated for clarity)

sweep the laser's frequency via the PZT, the cavity registers a peak in transmission each time the frequency is a multiple of the the etalon's free spectral range (FSR). Over the course of a scan through the atomic absorption, we record the cavity transmission (Figure 4.4), which reflects the PZT nonlinearities. This gives us frequency markers spaced by the FSR. We can fit these data very well using the usual Airy function for the cavity transmission, where frequency (ω) is replaced with a polynomial in voltage (Equations 4.1 and 4.2). In essence the polynomial is a fit to Figure 4.3, giving us a means to convert the the voltage at each point to a frequency.

$$T(\omega(V)) = \frac{a_0 + a_1 V}{1 + \left(\frac{FSR \sin[\omega(V)\pi/FSR]}{\pi FWHM}\right)} + a_2 \quad (4.1)$$

$$\omega(V) = a_3 + a_4 V + a_5 V^2 + a_6 V^3 \quad (4.2)$$

The accuracy of this fit is limited by our knowledge of the cavity's FSR and by its stability. Fortunately we have high confidence in each of these. The cavity is manufactured by Burleigh and constructed of Super-Invar, a material with an especially low thermal expansion coefficient (10^{-7}/C). For our needs, the temperature should be constant to within 1°C ([Fri01]), a condition easily met by surrounding the etalon with acoustic insulation for passive temperature control. With the cavity stabilized, we can measure its FSR with great precision , using a bootstrapping method:

1. Carefully measure the cavity length for an initial guess for the FSR. (Since we have a confocal cavity, the relevant formula is $FSR = c/4l$, where l is the separation of the mirrors.)

2. Tune the laser to an etalon transmission peak; record the wavelength indicated by the wavemeter.

3. Go to a different transmission peak, many fringes away; note the new frequency and find the difference (Δf) from step 2. This Δf must be a multiple of the *real* FSR.[2]

4. Divide Δf by the old estimate of FSR (and round) to get the number of transmission peaks (n) that lie between the two frequencies measured insteps 2 and 3.

5. Divide Δf by n to get a new guess for the FSR.

6. Return to step 2 and repeat as desired, using progressively larger values for Δf.

By iterating this process previous students quickly converged on a value of 500.0(1)MHz for the FSR. With the fit complete, we can linearize the frequency scan and accurately assign frequencies to each point on the scan through the atomic absorption.

In the future, as we proceed to make measurements of the Stark shift and Stark induced amplitudes, we will probably use the cavity to "lock" the frequency of the diode laser as was done in the past. In this mode of operation, we actively scan the Fabry-Perot cavity with a piezo, and measure the transmission of the diode laser as well as a second temperature stabilized HeNe laser. The frequency of the HeNe output is both well known and constant, so it acts as reference against which we can compare the fluctuations of the diode laser. A computer continuously monitors the relative positions of the HeNe and 1283nm diode peaks and compensates for the movement by sending a signal back to the diode PZT. This transfers the stability of the HeNe to the diode laser via a feedback loop. This technique will limit frequency fluctuations in the diode laser to less than 1.3MHz RMS. For a more detailed explanation of how this works and information on our software implementation, see [Spe00].

[2]It is insufficient to measure the change in frequency over one FSR because the wavemeter's resolution is 10MHz at best.

4.1.3 The Electro-Optic Phase Modulator

The electro-optic modulator ("EOM" in laboratory parlance) is the heart of the two-tone technique; this device that modululates the phase of the laser as it passes through the crystal and resonant cavity. It should be no surprise that an EOM works by means of the electro-optic effect, but since this unhelpful to the uninitiated, I shall attempt a better one.

Within some crystals, the index of refraction is sensitive to an applied electric field, a phenomenon known as the "electro-optic effect" or "Pockels effect." The electric field induces a birefringence, preferentially slowing light polarized along one of the crystals axes. This effect lends itself to a wide variety of applications, from optical communications, and phase modulators to amplitude modulators, q-switches and lightning detectors. When using as a phase modulator as we do, one orients the crystal, electric field and polarization so that they are all in the same plane. (See Figure 4.5) The electric field increases the index of refraction for light polarized in this plane according to

$$\Delta n = \frac{n_0^3 r E}{2}, \tag{4.3}$$

where n_0 is the unperturbed index of refraction, E is the external electric field and r is determined by the electro-optic properties of the crystal. In some materials, such as lithium niobate $LiNbO_3$, which is used in our EOM, the effect (i.e. r) is especially large. As the laser passes through the crystal, the phase of the emergent wave is determined by the strength of the electric field. The total phase shift imparted to the laser (relative to the zero field case) is determined by the laser wavelength (λ), the length of the crystal (l), voltage across the field plates (V) and separation of the plates (d) as shown below.

$$\Delta\phi_{EOM} = \frac{\pi n_0^3 r l V}{\lambda d} \tag{4.4}$$

If V oscillates, as it does in our laboratory, then the phase of the emergent wave will also oscillate. By definition, this is frequency modulation, although purists will observe that this is strictly phase modulation; however, the two are essentially the same, as discussed in Section 3.2. In our setup, we send two nearby radio frequencies (RF) to the EOM. Our means of creating these two frequencies are described in Section 4.1.4. Following the "two-tone modulation" in the EOM the electric field of the laser is

$$E(t) = E_0 \sin(\omega_{laser} t + \Delta\phi_{EOM}), \tag{4.5}$$

where

$$\Delta\phi_{EOM} = \beta_+ \sin\left(\omega_m + \frac{\Omega}{2}\right) + \beta_- \sin\left(\omega_m - \frac{\Omega}{2}\right) \tag{4.6}$$

and the β's encapsulate the constants in Equation 4.4.

In order to maximize the demodulated atomic signal, we want $\beta_- = \beta_+ = 1.08$ (See Section 3.4); however, here we encounter the practical problem of generating large electric fields. Our application requires fields much stronger than an average

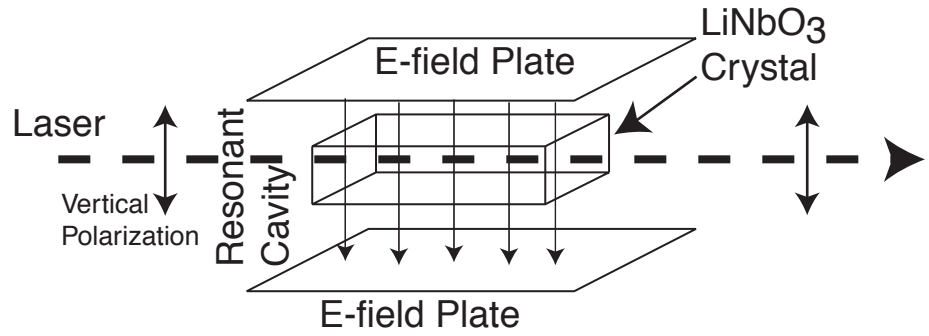

Figure 4.5: Inside the EOM (after New Focus product manual, [New01])

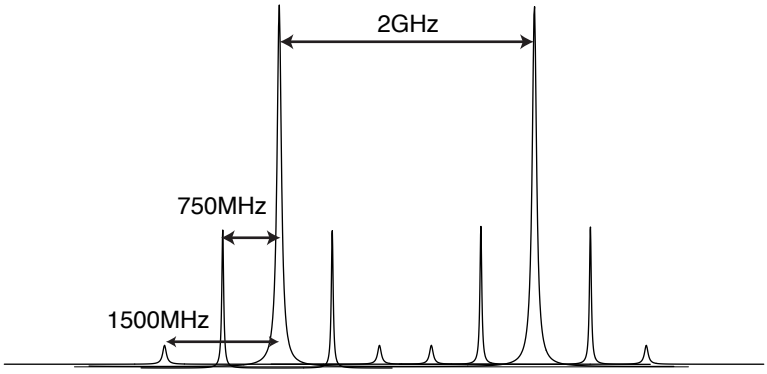

Figure 4.6: Optical Spectrum Analyzer signal, showing 750MHz and 1500MHz sidebands (simulated)

frequency synthesizer or amplifier can produce. Placing the crystal within a resonant cavity and circuit reduces the power needs to a reasonable 4W. New Focus tuned our model to our desired frequency of 750MHz prior to sale. This frequency tuning is approximate at best. The unit constantly dissipates 4W causing its temperature to rise dramatically when turned on. This temperature change causes the EOM the resonance to drift as much as 1.5MHz. Fortunately the resonance stabilizes as the unit reaches thermal equilibrium. Like the laser and Fabry-Perot etalon, the EOM lives within an acrylic box insulated with acoustic foam to keep its temperature stable. Once the unit has come to thermal equilibrium, the resonant frequency remains stable to within 0.1MHz over a period of hours, with a FWHM of about 2MHz. We are still concerned about this frequency drift because the cavity resonance is only a few MHz wide and we are modulating at two frequencies separated by 2MHz. We want to keep the modulation depths (the β's in Equation 4.6) equal so that our fitting functions, based on the theory in Section 3.4, are applicable.

Following the EOM, we use an optical spectrum analyzer to measure and optimize the RF modulation depth. A flipper mirror selects whether beam goes to the analyzer or the atoms. The spectrum analyzer is a high-finesse (>300 if you're both patient and lucky) confocal Fabry-Perot interferometer manufactured by Burleigh (model SA-200). Figure 4.6 shows a typical scan of cavity transmission when the EOM is operating well. (Since we display the spectrum analyzer output on a low-tech, pre-GPIB TDS scope, the figure is a simulation.) The 2GHz free spectral range cavity easily separates the upper and lower 750MHz RF sidebands from the optical carrier, as well as the second order sidebands 1500MHz away from the carrier, but it cannot resolve the two RF frequencies separated by 2MHz. To maximize the modulation depth in the EOM, we adjust the RF carrier frequency several MHz around the EOM's nominal 750MHz resonance, stopping at the point where the spectrum analyzer shows the greatest cumulative power in the sidebands. At present, our best modulation depth is $\beta_+ \approx \beta_- \approx 0.7$, as determined by the ratio of the heights of the sidebands to the carrier in the spectrum analyzer. This gives us 85% of the maximum demodulated signal strength when $\beta = 1.08$.

4.1.4 Frequency Sources

The EOM requires two closely spaced frequencies as inputs. As mentioned above, we use two frequencies spaced by 2MHz and centered on the EOM resonance (750±1MHz). We generate this waveform in several steps. First an HP 8656B RF synthesizer generates a pure sinusoid

$$E_{RF}(t) = E_{0,RF} \sin(\omega_m t). \tag{4.7}$$

Simultaneously a stable SRS DS335 function generator produces a low frequency (LF, in radio jargon) 1MHz wave.

$$E_{LF}(t) = E_{0,LF} \sin(\frac{\Omega}{2} t + \phi_0) \tag{4.8}$$

For consistency with the notation in Chapter 3, I use Ω for the detection frequency and $\Omega/2$ =1MHz for the LF.

These combine in a frequency mixer (Mini-Circuits model ZLW-2H) to produce the two frequencies $\omega_{RF} \pm \omega_{LF}$. An ideal frequency mixer works by simply multiplying the two input waveforms

$$\begin{aligned} E_{out}(t) &= E_{RF}(t) \cdot \sin(\frac{\Omega}{2} t + \phi_0) \\ &= E_{0,RF} \sin(\omega_m t) \sin(\frac{\Omega}{2} t + \phi_0) \\ &= \frac{E_{0,RF}}{2} \left[\cos\left((\omega_m - \frac{\Omega}{2}) t - \phi_0 \right) - \cos\left((\omega_m + \frac{\Omega}{2}) t + \phi_0 \right) \right], \end{aligned} \tag{4.9}$$

but there are nonlinearities in the circuit which depend on the LF power and introduce higher harmonics (i.e. $\omega_{RF} \pm 2\omega_{LF}, \omega_{RF} \pm 3\omega_{LF}, \ldots$) and some bleed through of the RF

frequency (ω_{RF}). These frequencies have at least 10dB less power than the desired ones. Varying the RF and LF power into the mixer adjusts the relative amounts of power in the first order mixing frequencies (the desired $\omega_{RF} \pm \omega_{LF}$) versus the undesired RF carrier and higher order mixing terms. In general the total output power scales with the RF power and the LF power is proportional to the amount of mixing. Only if the LF power is much higher than its specified limit do the higher order harmonics become significant. For our puposes more LF power is better; higher order mixing terms lie outside the range of efficient frequencies for the EOM. The frequency mixer is a robust device, which can be safely operated well beyond its quoted frequency and power specifications, albeit with reduced efficiency.

For greatest modulation depth, the EOM requires 4W of RF power. This is orders of magnitude greater than what the HP synthesizer can produce, so we have a Mini-Circuits RF amplifier (model ZHL-1000-3W) between the mixer and the EOM. While the amplifier's gain is nominally 37dB, the actual gain is closer to 45dB. Since excessive power damages the crystal and causes horribly debilitating RAM, one must carefully check and double-check whether the RF power going into the EOM is within specifications.

4.2 Atoms

With the two-tone modulation complete, the laser light moves on to the atoms. Using a flipper mirror we choose whether the light goes to the vapor cell or the atomic beam. A mechanical switch box determines which photodetector output goes to the lock-in amplifiers, oscilloscopes and computer.

4.2.1 Vapor Cell

The vapor cell was used in two previous previous experiments. One culminated in a measurement of E2/M1 by Leo Tsai and the other found a new value for the isotope shift in the $6P_{1/2} \rightarrow 7S_{1/2}$ transition. Leo Tsai and his predecessors described the behemoth in great detail ([Tsa98]); I refer the reader to their work for details of its construction. In the vapor cell's current incarnation, we have modified and generally simplified the unit, so I will summarize its basic function and our changes.

The heart of the vapor cell is a 15cm long quartz cell containing thallium. As Figure 4.7 shows, the ends of the cell are constructed with wedges to eliminate reflections and possible etalon effects. A small stem protruding from the base of the cell contains several milligrams solid thallium that vaporize at high temperatures and diffuse upward where the atoms interact with the laser.

A large mass of heating elements, insulation, water cooling tubes and mu metal surround the cell. These components serve to keep the cell hot, while the outside remains only slightly above room temperature, as long as the water continues to flow. Figure 4.8 shows a cutaway view of the oven and shielding, indicating where the heating and cooling elements are located. Also noted are the magnetic fields coils that

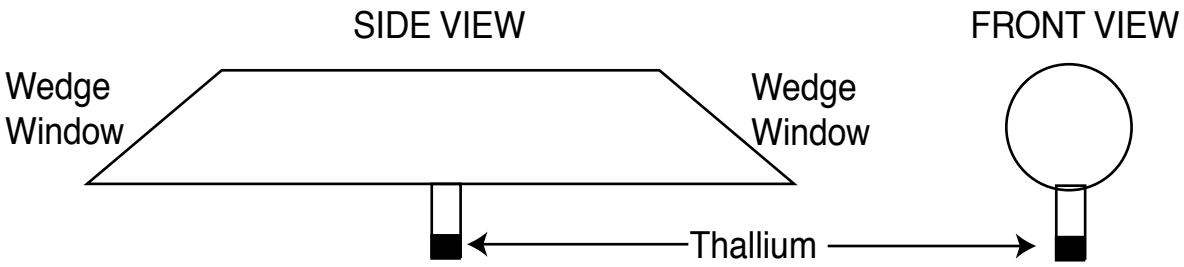

Figure 4.7: Thallium Vapor Cell (from [Tsa98])

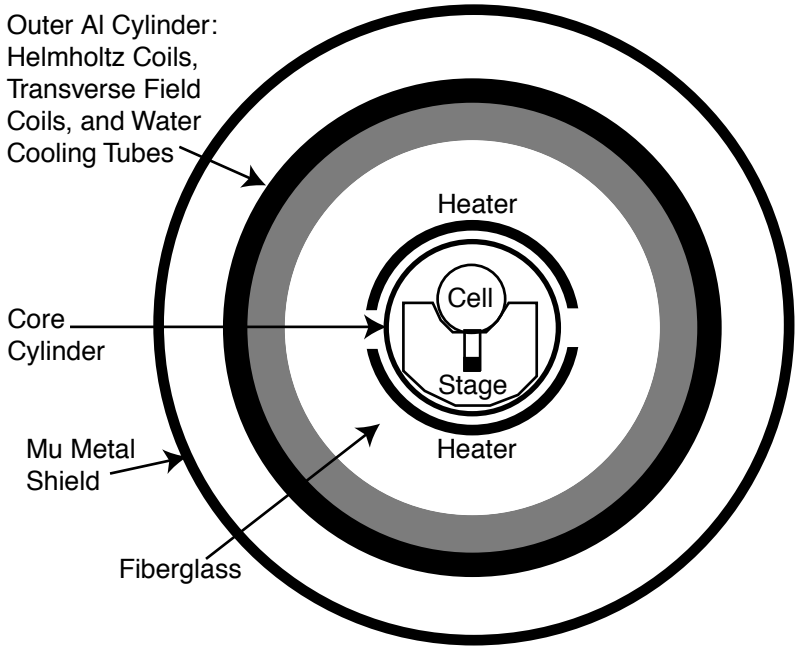

Figure 4.8: Oven cross-section (from [Tsa98])

were formerly used for generating Faraday rotations, but now remain dormant and the ceramic stage which holds the cell in place. There are several thermocouples distributed throughout the unit that are not shown. These monitor the cell temperature and the temperature in the surrounding insulation.

Four clam shell heating units surround the core ceramic cylinder (which contains the cell). Combined, these heating elements are 30cm in length, so any longitudinal temperature gradients in the 15cm vapor cell are small. By maintaining a uniform temperature, we avoid complications due to non-uniform thallium densities or the problem of thallium coating the windows.[3] We control the temperature through the primitive regulatory mechanism of heat flow. The four heating elements of the system are grouped into two pairs wired in parallel. A Variac powers each of these pairs. To

[3]Recently we have seen increased thallium deposits on the windows, which could cause anomalously high absorption or block the signal entirely. Presently, we aim the laser at a thallium-free section of the window.

reach a stable temperature, we simply set the voltage for each heating element, then wait for the system to equilibrate. In general, our present work does not require great temperature stability or precision control; we only need a sufficiently hot environment to vaporize the thallium so we can see an absorption and confirm that our optical and detection systems are functioning.[4]

The core cylinder is sealed at both ends with aluminum endcaps that each have AR-coated windows. On one end a vacuum fixture connects the cylinder to a mechanical vacuum pump and vacuum gauge. This crude vacuum system will hold pressures of order 1Torr, but every few hours someone must run the vacuum pump for a few minutes to maintain the vacuum. The vacuum has two purposes: 1) It speeds the process of heating the vapor cell. 2) It reduces air currents within the core cylinder which could affect the laser path and intensity via index of refraction changes.

4.2.2 Atomic Beam

The recent Stark-shift measurement completed by Charlie Doret demonstrates the advantages of the atomic beam unit (ABU) over the vapor cell. Taking advantage of the narrow Doppler features in the atomic beam, Doret measured a 50MHz frequency shift to an accuracy of ¡0.5% [Dor02]. The trick making this possible is collimation. Like the vapor cell, the ABU produces atoms by heating solid thallium; then they must pass through a series of razor blade collimators (Figure 4.9) that ensure the atoms move in a direction transverse to the laser beam. If the collimation were "perfect" and all atoms travelled perpendicular to the laser, there would be no Doppler broadening, but there would also be no atoms in such a beam. The geometry of the collimators determines both the atomic density as well as the beam divergence. Thus we can reduce the beam divergence, and consequently the Doppler width, by narrowing the slits, but this also decreases the number of atoms in the beam. In any case, the beam density is low enough that there are extremely few atomic collisions and no measurable lorentz broadening of the absorption.

The details of construction and components are described in past theses, so I refer the reader to those documents. Aside from the modifications mentioned below, the ABU remains as described by [Nic98], [Fri01] and [Dor02].

A new thallium oven and heat shielding have been in use for the past year. While the new scheme maintains the same overall shape and orientation of the oven as the old scheme, a new method for wrapping the thermocoax provides better thermal contact over a greater length of thermocoax. The old wrapping pattern was a zig-zag; in addition to less surface contact with the oven this design introduced kinks in the thermocoax. Burnouts tend to happen at sharp bends because these points have a low ratio of thermal contact to length. The new oven has a semicircular channel, of

[4]Tsai's and Lyman's experiments employed a variable-duty cycle heating system to control the cell temperature through a temperature feedback system which turned the heating elements on and off as appropriate to maintain the desired temperature. This system is still intact, so we could revive it if desired.

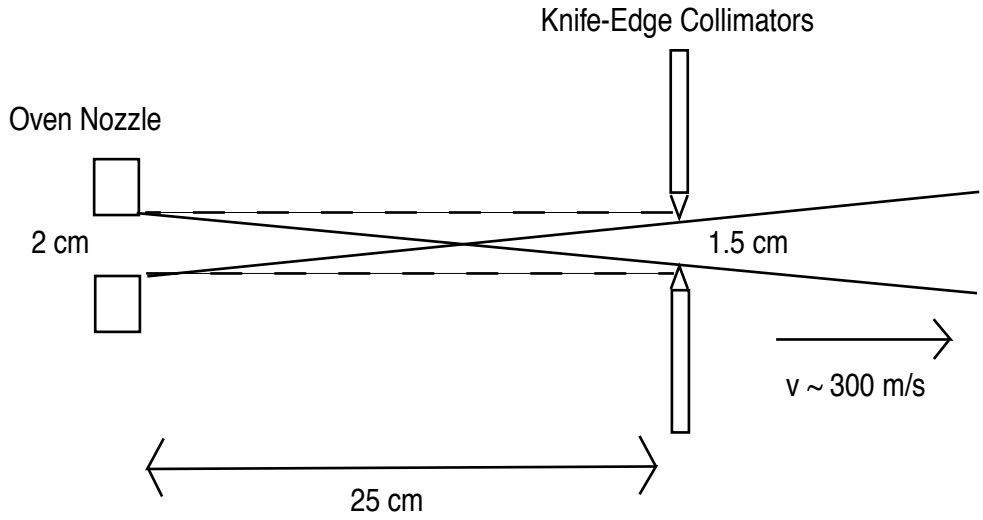

Figure 4.9: Razor blade collimators (from [Dor02])

the same diameter as the thermocoax, machined in a tight spiral around the body and nozzle. Two different segments (lengths 475cm and 100cm) sit in these grooves to heat the body and nozzle. Given their lengths and thermal contact, the voltages applied to the body and nozzle heaters should not exceed 120V and 27V, respectively. Both elements are secured and forced against the oven with sheets of 1/16" stainless steel and stainless hoseclamps. (See Figure 4.10.) As before, separate thermocouples monitor the temperatures of the nozzle and body. In addition, we added a thin layer of molded stainless steel heat shielding (shown as dashed line) between the oven and the 1/8" thick "box" that surrounds the oven. Together these changes lower the operating voltages required for a given oven temperature and allow us to reach higher oven termperatures and, hence, greater beam densities.

Chopping the atomic beam is an ongoing technical challenge. Ideally one would modulate the atomic beam at several hundred hertz and demodulate the absorption signal at this frequency. This would remove low frequency noise and serve as an additional normalization. In particular, chopping the atomic beam would remove any RAM background. Rotating a shaft at 1500rpm requires requires ball bearings, but the high-vacuum and high-temperatures of the ABU are formidable operating conditions for most bearings. We are presently trying a new bearing assembly constructed with ceramic (silicon nitride) balls (for high-temperature) impregnated with tungsten disulfide (for low-vapor pressure lubrication). The chopping wheel and its mounting plate is nearly identical to past versions, but with greater adjustability. Even with careful alignment, mechanical vibrations transferred to the vacuum chamber and optics continue to be a problem. We are reducing these with a new, heavier stainless steel plate for mounting optics and several different kinds of isolation.

The two watchwords of this research are "precision" and "sensitivity." We need to make precise measurements if our work will have any scientific merit, but first

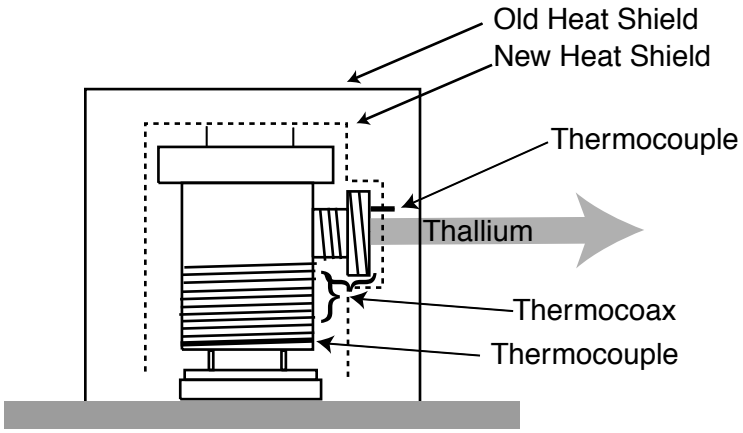

Figure 4.10: New spiral thermocoax wrapping pattern on body and nozzle. New 1/16" stainless heat shield.

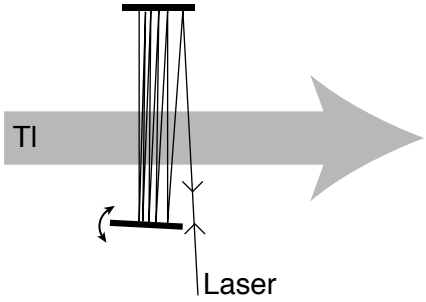

Figure 4.11: Mirrors for laser multipass.

we need to be "sensitive" enough to observe the atoms. We are developing a mirror configuration which will direct the laser through the atomic beam multiple times before going to the photodiode detector. This effectively increases the interaction length and, consequently, the optical depth. If we can multipass the laser 20 times, we will see a 20–fold improvement in our sensitivity. Figure 4.11 shows one possible implementation in which one adjustable mirror controls the number of passes the laser makes through the beam. As the laser reflects back and forth, it "walks" across the mirror, and eventually retracing its steps back out. Appendix B discusses more of the technical issues with this idea.

Long ago in the design phase of the ABU, Peter Nicholas had the foresight to realize that the collimators reject a lot of thallium that could be recycled. Most of the thallium collects in the containment cone that follows the oven nozzle. This cone was designed to sit atop the oven with its top removed, so the thallium would drain out when heated. Last summer the inner containment cone was full for the first time in the life of the ABU, so it was time to put the design to the test. When the original recycling procedure didn't work, we removed the outer containment cone and wrapped the inner cone in aluminum foil (a makeshift heat shield) atop the oven.

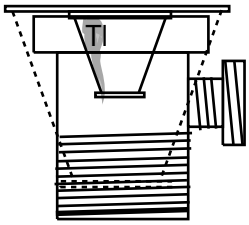

Figure 4.12: Remove outer containment cone and invert over oven to recycling thallium.

After heating the oven to 500°C nearly all of the nasty[5] thallium returned to the oven. Figure 4.12 illustrates the way we did this.

4.2.3 Optical Depth (Vapor Cell vs. ABU)

The drawback of the ABU is its low atomic density. The collimation process rejects all atoms except those few in the Maxwell-Boltzmann velocity distribution that happen to fall within a narrowly specified solid angle perpendicular to the laser. The low atomic density accentuates the problem of the small absorption cross-section for this transition, but our two-tone detection method was specifically designed with sensitivity in mind. Nevertheless, when one fails to see a signal in the ABU on the first try, one doesn't know where the problem lies. We would like a means of determining whether our detection scheme is working sufficiently well that we *should* see something in the ABU. The vapor cell is ideal for this purpose. We can compare the optical depths for the two atom sources with the formula

$$\delta(\omega_0) = Nl\sigma_0. \tag{4.10}$$

In this case, ω_0 is frequency of the absorption peak and σ_0 is the corresponding absorption cross-section. Section 2.3 discusses the components of this equation in greater detail, but the results are encapsulated in Figure 4.13. The plot shows the optical depths for the ABU and vapor cell as a function of temperature. While temperature does not appear explicitly in Equation 4.10, it is implicit in both the density N (through vapor pressure). For the vapor cell, we can find the number density using the ideal gas law with the vapor pressure. In the atomic beam, we must reduce this density by factor representing the solid angle through which the atoms

[5]There is a clear precedent in the thallium literature that requires the writer to comment on the dangers of thallium exposure. Since this information is relentlessly rehashed, I will relegate it to a footnote. Like its periodic neighbor lead, thallium is a toxin that compromises the nervous system. That it was used as a rat poison prior to a 1972 law banning this use should tell you something about its toxicity. Its pernicious superpower is that it can be absorbed through the skin, so one must use great care when working around the metal. Fortunately, its biological half-life is short, on the order of 10 days, so minimal exposure over a long period of time is relatively safe. Our standard precautions are to wear gloves and lab coats when working inside the ABU, and wash our hands afterwards.

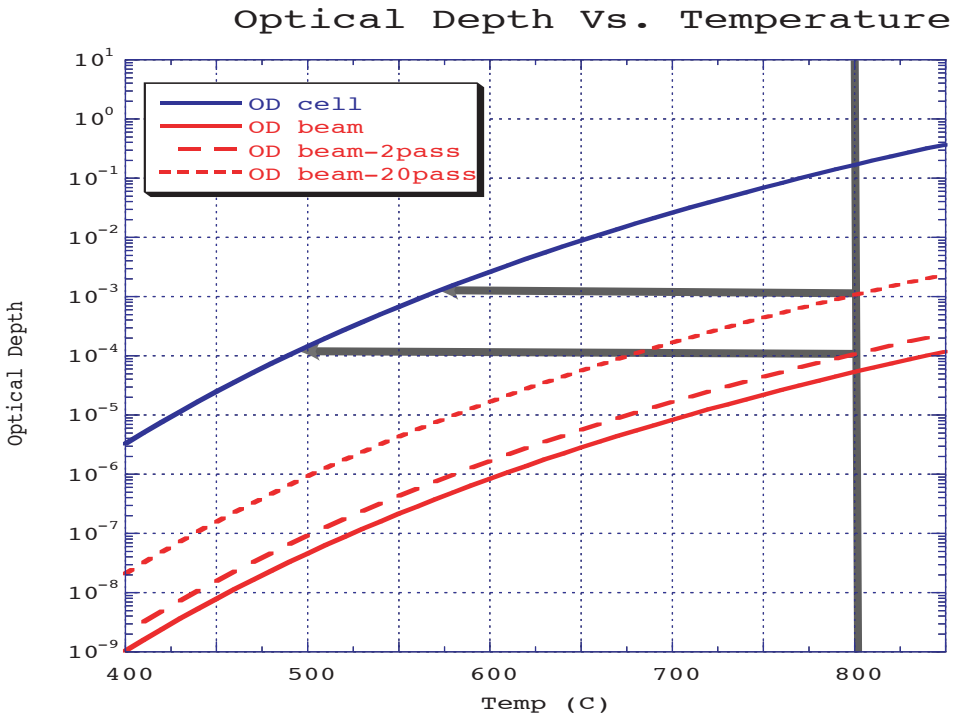

Figure 4.13: Comparison of Optical Depth in the Vapor Cell and ABU, using single and multiple passes of the laser. Horizontal and vertical lines are for reference.

can escape the oven. The temperature dependence of σ_0 is less obvious. Consider a fixed number of thallium atoms at high and low temperatures. At low temperatures, there is little Doppler shift, so nearly all atoms see the light as on resonance. At high temperature, they have a wide doppler spread, which "depopulates" the resonant state as it fills ones with higher velocity. One can show that $\sigma_0 \propto \frac{1}{\Delta}$ (See Equation 2.12), and thus this term is also temperature dependent. For the atomic beam Δ is determined by the beam divergence rather than the temperature exclusively. This means that the Doppler width for the ABU is much smaller than that of the vapor cell, but still nonzero. Consequently, the ABU has a greater absorption cross-section on resonance.

We can combine the temperature dependent effects with the known interaction lengths in the ABU and vapor cell, to get the optical depth in each. The graph shows the maximum possible optical depth in the ABU, given several different numbers of laser passes through the interaction region and a maximum oven temperature of 800°C. Also shown are the possible increases in optical depth from multipassing the laser through the ABU interaction region. By looking for absorption in the vapor cell at the temperature with the equivalent optical depth (i.e. setting the vapor cell to ∼500°C), we can assure ourselves that the optical and detection systems are working properly and with sufficient sensitivity that we ought to see evidence of absorption in the atomic beam.

4.3 Detection Components

Having gone through the work of cajoling the laser light into the proper frequency spectrum and providing generous numbers of atoms to interact with the light, we naturally want to see some results. We have a high-speed photodiode after both the vapor cell and the ABU and several lock-in amplifiers, all described below. A three position switch selects which atom source goes to the lock-in and scopes, provided one remembers to put the flipper mirror in the proper position! We can use the vapor cell to confirm that the laser is operating at the correct wavelength, then switch to the atomic beam to search for a signal.

4.3.1 Photodiodes

Infrared semiconductor photodiodes (made of indium-doped gallium arsenide, InGaAs) are comercially available with response times as fast as a 0.1ns. We use New Focus' more modest model 1811, which has a maximum frequency response of 125MHz. This is well above the 2MHz range that we need for our detection. Because the diode saturates with a laser input power of 120μW, one must guard against saturating the detector. While no amount of power from our laser will damage the photodiode, saturating the detector makes it impossible to see any absorption, demodulated or otherwise. For the benefit of anyone using these detectors, two hints that a detector is saturated are: 1. a photodiode output of 3V 2. a steady lock-in signal of zero.

4.3.2 Lock-in Amplifiers

We use lock-in amplifiers in two steps, as indicated in Figure 4.14. First an SRS844 RF lock-in amplifier demodulates the photodiode signal at 2MHz. This model operates at frequencies up to 200MHz. Aside from the higher operating frequency, this model is almost identical to audio lock-ins, except that it features nearly twice as many lights as the more mundane SRS810. This makes it *much* more impressive with the lights off, although I recommend having several of the older lock-ins on as well if you really want to dazzle an audience. A very convenient feature of SRS844 unit is the "2f" input. In this mode, the detection frequency is twice the reference frequency input. We use the 1MHz output from the SRS function generator, which also feeds into the frequency mixer, as the reference and detect at 2MHz. The DC offset also comes in handy for eliminating background signals, such as RAM. First, detune the laser from the transition, set the DC offset to zero the signal, then return to the absorption of interest. For a brief review of phase sensitive lock-in detection, see [Spe00].

When chopping the atomic beam, a second lock-in acts as a further normalization. While we are not yet using this second stage of lock-in detection, we almost certainly will in the (hopefully near) future. An SRS810 audio lock-in amplifier triggers from a photogate that monitors the chopping frequency. When using two lock-ins in se-

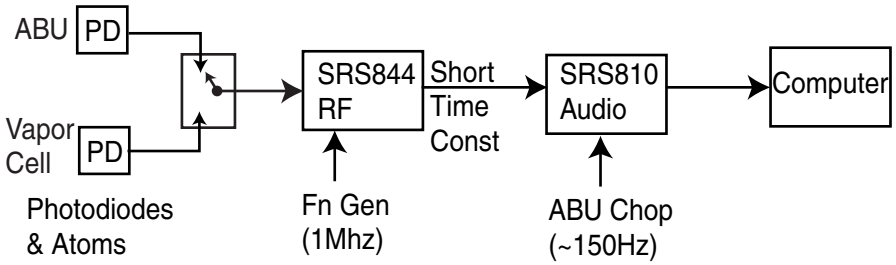

Figure 4.14: Flow Chart of Signal Processing.

quence, one must be careful to set their time constants appropriately.[6] Let's say the beam chopping frequency is F_{chop}. Now the corner frequency from a lock-in is set by the output low-pass filter time constant. $F_{corner} = \frac{1}{2\pi\tau}$, where τ is the time constant. Thus we have the important criterion that

$$\tau \geq \frac{1}{2\pi F_{chop}}. \tag{4.11}$$

Therefore, if the beam chopping frequency is a reasonable 150Hz, the RF time constant should be $\leq$1ms. With the SRS844, one must be a little more careful because the F_{corner} given above, refers to the -3dB point for a single low-pass filter, but this fancy unit has additional output filters that increase the roll-off per octave (in multiples of 6dB/oct.). One can choose one through four filters so that F_{corner} is the -3ndB point, where n is number of filters chosen. This means that a high roll-off will require a longer time constant to pass the same amplitude of F_{chop}.

4.4 A Typical Scan

The entire data collection process is conducted by a computer, using the body of C++ code established by previous students. Since we are using a new SRS844 lock-in amplifier we created a new interface class to control it via GPIB, based on the preexistent SRS810 code. We also added new member functions to both lock-in classes so that the computer can read and change the lock-in sensitivity and time constant.

A scan consists of the computer ramping the voltage on a single analog output channel while simultaneously reading information on numerous analog and GPIB channels. The voltage goes the the laser PZT bias input, generally with a resistive voltage divider mediating. The voltage output is set by a digital-analog converter which cannot take steps smaller than a few millivolts. This step size corresponds to nearly ten megahertz in laser frequency. We typically want finer frequency resolution, which a voltage divider does very easily, by reducing the effective step size to a

[6] I repeat this simple derivation because it is useful to know, but eminently forgettable where the 2's and π's belong.

fraction of a millivolt. For the results in the next chapter, we swept the laser over six gigahertz, enough to include the doppler broadened vapor cell spectrum, plus all significant sidebands, corresponding to a computer voltage range of 2V. The input side is more complicated, so I will first list the inputs, then return to discuss the most important ones in more detail.

1. Demodulated photodiode signal– either from ABU or vapor cell
2. Etalon transmission
3. Normalization photodiode voltage
4. Temperatures– ABU oven and vapor cell temperatures measured via SRS630 themocouple monitor

As discussed in Chapter 4, a photodiode measures the light transmitted through the sample and this signal is demodulated at 2MHz in the SRS844 lock-in amplifier. The user must adjust the lock-in sensitivity appropriately for the vapor cell temperature, then send the lock-in output into an analog input. For each point in the scan the program averages 10 readings from the lock-in, etalon and normalization photodiode. The data collection program writes point number, demodulated signal, etalon transmission, normalization voltage and temperatures to a file for processing later.

Chapter 5

Data & Future Data

This is a work in progress. To date we have demonstrated the feasibility of the two-tone detection technique in the atomic beam, using the vapor cell, and essential first step toward our eventual goals. We hope to begin measurements of the isotope shift, Stark shift and Stark induced amplitudes during the coming summer. This chapter discusses our data analysis routines and presents results on which we are staking our confidence in the atomic beam.

5.1 Frequency Calibration

Following the data collection process described in Chapter 4, we must convert the voltage scan to frequency, removing nonlinearities. We do this by first fitting the etalon transmission to an Airy function, as discussed in Section 4.1.2. The fitting function initially converts the point numbers (numbers `i = 1 - npoints` to a "normalized point number," so that each data point is assigned an value between -1 and 1 according to $\texttt{xx} = \frac{\texttt{i}-\texttt{npoints/2}}{\texttt{npoints/2}}$. We then fit the Airy function with a polynomial in `xx` that represents the laser's nonlinear frequency response to the PZT voltage. The fitting routine can use a polynomial up to order 8, but we find no advantage in using more than the cubic term. By normalizing the point number, we can easily compare the relative sizes of linear, quadratic and cubic terms in the PZT response. Because of hysteresis, the scans up and down in frequency are fit separately. With this fitting done, we have a map from point number to frequency, albeit with an arbitrary frequency of zero at `i = npoints / 2`. Since measurements of isotope shift and Stark shift are relative frequencies, it is unimportant what the absolute frequency is for any point in the scan.

5.2 Vapor Cell Data

We have collected numerous scans of the demodulated two-tone signal in the vapor cell. Figure 5.1 shows a scan at a high temperature, where the signal to noise ratio

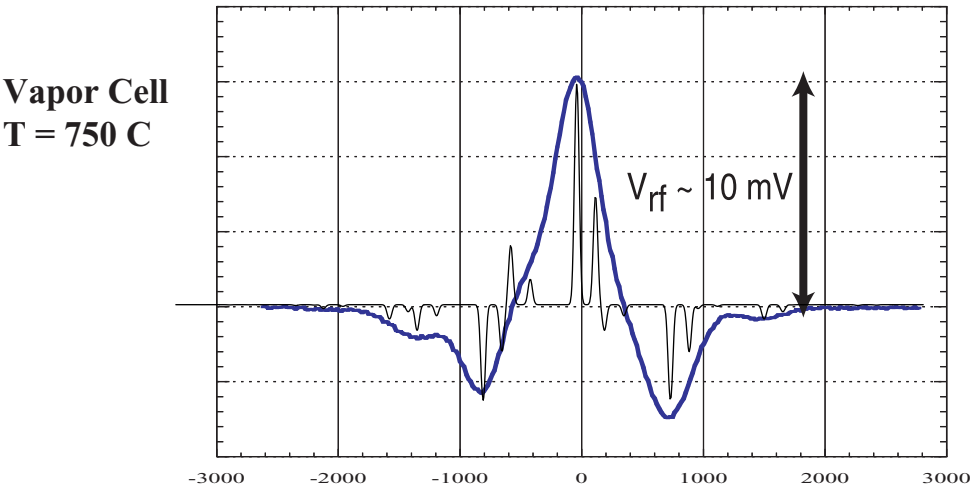

Figure 5.1: Experimental vapor cell scan (initial state $6P_{1/2}F=1$) with simulated ABU scan overlaid.

is especially good. It is difficult to interpret this curve because the Doppler widths are approximately the same as the hyperfine splittings and much greater than the isotope differences. Overlayed on the vapor cell data is a theoretical simulation of the same scan conducted in the ABU, with narrow Doppler features. The spacing of the absorptions and their inverted sideband images in the theoretical curve give an indication of why the vapor cell data are so asymmetric. Note that the second order sidebands are are visible in both the theoretical and measured spectra, a feature that would not be present if the modulation depth were lower.

We have our eye towards moving to the atomic beam, which has much lower optical depth than was used for this clean scan. As Figure 4.13 indicates, if we are going to have any hope of seeing something in the atomic beam, we should be able to detect absorption in the vapor cell at temperatures in the range of 500-550°C, depending on how many passes the laser makes through the ABU interaction region. We already have data from this regime, reproduced in Figure 5.2. The signal size drops so dramatically with temperature because the vapor pressure of thallium is an exponential function of T. The low temperature scans also exhibit more narrow Doppler features than the scan at 750°C. (The horizontal displacement in frequency between the various scans is simply a consequence of the fact that each scan started at a slightly different absolute frequency.)

5.3 Absorption Fitting

In the future, when we attempt to measure the isotope shift and Stark shift we will need fitting routines that use these quantities as fit parameters. From previous work we have accumulated a software library for this purpose. These routines use a Levenburg-Marquardt non-linear least squares algorithm to fit our demodulated

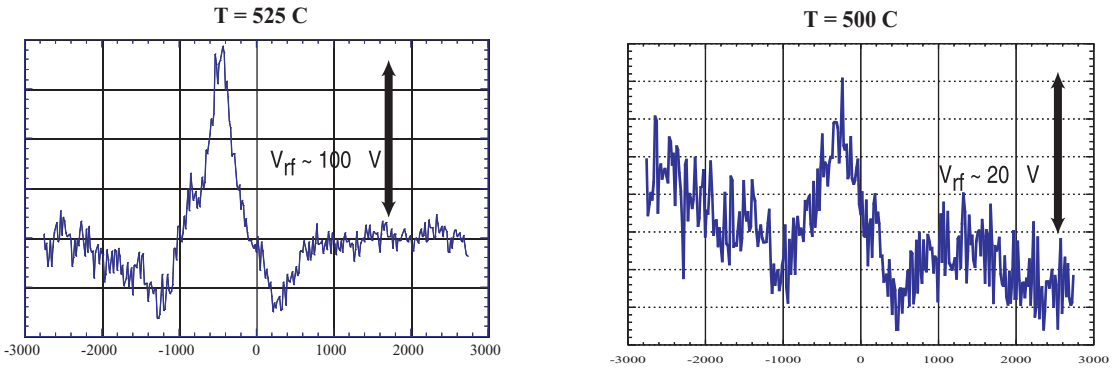

Figure 5.2: Vapor Cell scan with optical depth equivalent to ABU.

scans. For the atomic beam, the functional form of the fitting function is a relatively straightforward sum of gaussians, with relative amplitudes specified by the values of the modulation depth ($\beta_{\pm}$), isotope abundance, hyperfine degeneracy and well-known quantum mechanical transition amplitudes for E2 and M1 transitions. When use the modulation depth as a fit parameter, we must deal with the problem of how to calculate derivatives of the fitting function with respect to $\beta_{\pm}$. To increase the speed of the fitting routine, we use an approximation for the derivatives of Bessel functions. Since we know that $\beta \approx 0.7$, a linear expansion of the Bessel function in this viscinity is perfectly adequate and computationally fast.

Fitting the profile from the vapor cell is more complicated because the Voigt profile is a convolution of gaussian and lorentzian components. The fitting routine must be able to calculate trial functions quickly, so even numerical approximations to the integral are insufficient. We use an efficient series approximation to the Voigt profile (described in [Vet95]). We may also include extra fit parameters to remove linear and sinusoidal background trends in the data; these effects are present at all temperatures, but only noticeable at low temperature because the signal size is on the same order of magnitude as the background trends. The scan at 500°C in Figure 5.2 shows a significant linear trend; the effect is not due to laser intensity drift, because these data were normalized to the pre-absorption laser intensity at each point in the scan. Instead, this is probably a stray etalon effect due to a low Q cavity with a large FSR. (I say this with greater confidence than this plot alone supports because I know from other vapor cell scans that such etalon effects are common.) A coplanar cavity of 1cm or smaller in length will have a FSR greater than 15GHz, consistent with what appears in this figure. In fact there are many optical elements of this size in our setup, including windows, lenses and the EOM. We can hope to reduce any errors causes by these background effects by misaligning the optical elements slightly, as well as through good choice of fit parameters.

5.4 Future Steps

Much work remains before this project will come to fruition. With the laser modulation and demodulation system now firmly under control, we need to focus on the atomic beam. We have not yet detected signals in the ABU, so we are are taking the opportunity to improve the setup by installing mirrors so that the laser will pass through the atomic beam multiple times before going to the detector, effectively increasing the optical depth by a factor of 10 or more. After finding a black residue (possibly thallium oxide or thallium carbide) coating the inside of the ABU oven, we thoroughly cleaned the vacuum system to prevent a recurrence. If the substance was in fact thallium oxide, it may have remained solid at 800°C, lowering the Tl vapor pressure in the oven and, by consequence, the atomic beam density. Cleaning should therefore increase the atomic density in the beam.

In the near future, we will move to a new oven and vapor cell assembly. The new heating unit will be smaller because it does not need the bulky magnetic shielding and field coils.[1] Figure 5.3 shows a cross section of the new unit, with approximate dimensions. Like the previous cell, this one will be constructed from quartz to withstand high temperatures. The long evacuated extensions on either side of the thallium vessel will reduce heat induced index of refraction gradients without using a mechanical pump. The laser will enter the vacuum through a cool window, then pass directly into the thallium cell before repeating in opposite order to leave. The thallium is confined by internal partitions and heated to a uniform temperature to prevent deposition on the windows. The smaller total size of this unit is a major advantage because we will be able to move the oven and detection electronics on to the same optical table as the laser and other components, reducing any problems due to the physical drift of the tables.

Once we have a signal in the atomic beam, there is still much to do. First we must optimize the absorption signal. This means implementing the multipass arrangement, described in Appendix B, then finding the best is the geometric orientation of the laser and atom beams. This will involve finding the best combination of narrow Doppler features as well as large absorption. The chopping wheel and associated lock-in will require some adjustment as well to find rotation rates, time constants and vibration insulation that minimize noise that gets into the data, while still remaining

[1] In the meantime, the old vapor cell will find a yet another application as part of a new scheme to lock the diode laser frequency more precisely than we have done to date. Using the existing magnetic field coils, one can induce Zeeman splitting of degenerate m_F states. Since left and right circularly polarized light will excite different Δm_F transitions each at a different frequency, the indices of refraction for the two circular polarizations will be different. Therefore, incident linearly polarized light will experience a Faraday polarization rotation, which is dependent on laser frequency. The frequency where zero rotation occurs provides a lock frequency that depends only on the atoms and must be stable. Using this method, we hope to limit the frequency jitter of the diode laser to around 100 kHz. This degree of laser stability is important for long-term plans to search for an (unexpected) T-odd, P-even interaction in thallium. Preliminary work for this upcoming experiment, including design of a ring cavity, and construction of the locking system, continues in parallel with the research presented here. ([Maj03])

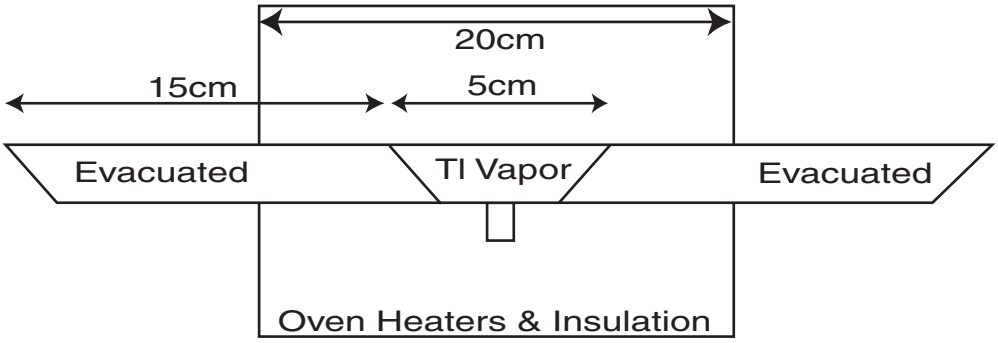

Figure 5.3: New oven and longer vapor cell.

fast enough to avoid the problems associated with long term drift.

With the signal in good shape, physically interesting measurements should soon follow. The isotope shift should be a relatively straightforward measurement. The shift should be well resolved in the ABU and since it appears multiple times in each scan due to the sideband images the fitting routine should have no problems finding it. For greater confidence in the validity of the method, it would be nice to verify measurements of χ, the ratio of electric quadrupole to magnetic dipole transition strengths (E2/M1). Quantum mechanics gives us a relatively easy way to measure χ. The relative transition strengths ($\mathcal{P}$) of $6P_{1/2}F = 1 \rightarrow 6P_{3/2}F = 2$ to $6P_{1/2}F = 1 \rightarrow 6P_{3/2}F = 1$ are related by

$$\frac{\mathcal{P}(F = 1 \rightarrow 2)}{\mathcal{P}(F = 1 \rightarrow 1)} = \frac{\mathrm{M1}(1 \rightarrow 2) + \chi^2 \mathrm{E2}(1 \rightarrow 2)}{\mathrm{M1}(1 \rightarrow 1) + \chi^2 \mathrm{E2}(1 \rightarrow 1)}. \tag{5.1}$$

The M1 and E2 amplitudes are individually calculable, so χ can be extracted from an experimental measurement of the relative transition strengths.

The next step will be to turn on the electric field plate for Stark shift and Stark induced amplitude measurements. This will require further planning regarding data collection. A particular absorption line must be chosen, as well as a method for measuring changes in amplitude. At this point the laser polarization relative to the static electric field ($\vec{\epsilon} \parallel \vec{E}_{static}$ or $\vec{\epsilon} \perp \vec{E}_{static}$) becomes important. Due to the tensor polarizability of the $6P_{3/2}$ F=2 state, a circumstance not found in the $6P_{1/2}$or $7S_{1/2}$ states, the m_F are *not* degenerate in an electric field. The laser polarization and selection rules determine which state the laser probes. Consequently, the Stark shift will be different for different laser polarizations. The shifts in each case will be interesting.

With data on the hyperfine structure, isotope shift and Stark effects, we will have a new round of precise data to compare with theoretical wavefunctions. Predictions of each measurement involve different sums of matrix elements, so every precise quantity that we can provide constitutes an independent check on the accuracy of existing electron, nuclear and particle physics models. Thus continues the virtuous circle of experimentalists and theorists trying to outdo one another in the attempt to refine physical theory.

Appendix A

Modulation Simulation

In Chapter 3, we derived the demodulated signal from absorption of a two-tone modulation. We might complain that the derivation is tedious, but its greater fault is that it is only approximate. In order to arrive at a tractable result (Equation 3.14), we stipulated:

1. The modulation depth (β) is much less than one.
2. The modulation depths are the same for both modulation frequencies.
3. Each pair of sidebands is absorbed equally. i.e. $\Omega \ll$ FWHM of the absorption.
4. The optical depth is much less than one.[1]

None of these requirements is strictly true. In particular, β is near 0.7 in our apparatus and this is clearly not "much less than one." Thus there are significant second and third order sidebands that modify the signal behavior. The other approximations are more appropriate. ($\Omega = 2$MHz, while the FWHM is $\sim$40MHz; $|\beta_+ - \beta_-| \ll 1$) Relaxing any of the assumptions is very difficult to do by hand because the number of terms that one must retain are myriad.

Nevertheless, we desire to model more precisely what the absorption *should* look like in our laboratory. Mathematica is an ideal, albeit slow and frustrating, tool for this purpose. While we could create numerical simulations of absorption profiles in numerous programming languages, Mathematica's symbolic manipulation feature gives us the functional form, as well as illustrative plots.

The difficulty of this programming task comes from Mathematica's parsing and sorting functions. While the mathematical operations treat equivalent expression equally (as they should), the parsing commands do not. For example, when sorting through an expression looking for terms of the form $e^{i(\omega_c+\omega_m+\Omega/2)t}$, Mathematica will find terms like $Ae^{i(\omega_c+\omega_m+\Omega/2)t}$, but not $Ae^{i(\omega_c+\omega_m)t}e^{i\Omega t/2}$ or even $Ae^{i(\omega_c+\omega_m)t+i\Omega t/2}$.

[1] In the atomic beam the optical depth is $\leq 10^{-4}$, so this assumption is reasonable, but in the vapor cell, the optical depth can be ≥ 0.1 at high temperatures. See Figure 4.13.

```
m1 = .7; m2 = .7;(* Choose degree of modulation, higher→ more sidebands *)
For[ModDeg = 1, (Abs[BesselJ[ModDeg, m]] > .05
    || Abs[BesselJ[ModDeg + 1, m]] > .05),ModDeg++];

E1 = TrigToExp[
  TrigExpand[
   ExpToTrig[
    Expand[
     (BesselJ[0, m1] +
        Sum[(BesselJ[n, m1] Exp[n I (w + Ω / 2) t]
             + BesselJ[-n, m1] Exp[-n I (w + Ω / 2) t]), {n, 1, ModDeg}])
      (BesselJ[0, m2] +
        Sum[(BesselJ[n, m2] Exp[n I (w - Ω / 2) t]
             + BesselJ[-n, m2] Exp[-n I (w - Ω / 2) t]), {n, 1, ModDeg}])]]]]
```

Figure A.1: Step One– Create the Electric Field Spectrum.

Therefore, one needs to find ways of forcing Mathematica to standardize its expressions. I accomplished this through rather unsightly combinations of `Simplify` and `Expand`, taking advantage of the different simplifying rules that Mathematica uses for equivalent exponential and trigonometric expressions. Each step of code that follows mimics what happens in a different part of our apparatus. All of the calculations are done in complex notation, without regard for numerical constants that multiply the entire expression. We can even leave off the laser frequency term ($e^{i\omega_{laser}t}$ or $e^{i\omega_c t}$) because this term drops out when we multiply by the complex conjugate to find the intensity at the detector.

In the block of code shown in Figure A.1, the user can select the modulation depths for the $\omega_m + \Omega/2$ and $\omega_m - \Omega/2$ frequencies. A `For` loop then calculates how many terms in the Bessel function expansion must be included and this stored as `ModDeg`. The current simulation retains all terms with Bessel coefficients greater than

```
imax = 2 ModDeg;
(* Include Primary modulation terms up to order imax
  (e.g. imax=1 include first sidebands only) *)
jmax = 2 ModDeg; (* Include Secondary modulation terms up to order jmax *)
For[i = -imax; E2 := 0, i ≤ imax, i++, For[j = -jmax, j ≤ jmax, j++,
  E2 += T[i][j] (Select[E1, (MemberQ[#, Exp[i I t w + j I t Ω / 2]] ) &])]]
E2 += T[0][0] (Select[E1, (FreeQ[#, w] && FreeQ[#, Ω]) &])
```

Figure A.2: Step Two– Assign unique transmission coefficients to each term.

```
Int = Chop[TrigToExp[TrigExpand[ExpToTrig[Expand[
      Conjugate[Expand[E2]] Expand[E2]]]]]]
```

Figure A.3: Step Three– Calculate intensity.

0.05. `E1` is the electric after the laser emerges from the EOM, with all significant frequency components retained.

In Figure A.2 the program mimics the atomic absorption. Each frequency term is given its own unique transmission coefficient. Mathematica assigns each term the appropriate transmission factor using pattern matching functions. `T[i][j]` is the transmission function $T(\omega_{laser} + i\omega_m + j\Omega/2)$ in the notation of Chapter 3.

Next (Figure A.3) we calculate the time average intensity of the laser. Once again, all the unsightly `Expand` and conversion functions are to coerce Mathematica to simplify the expression and group terms in the way any reasonable person would. I don't guarantee that this is the most efficient means to accomplish the task, but it's the only working method that I've found. At this step, Mathematica proves its worth. With `m1 = m2 = .7`, the expression for the electric field (`E2`) takes up most of a printed page and squaring that to find the intensity gives 27 pages of terms to sort and collect!

The code in Figure A.4 mimics the action of the lock-in amplifier. Only those terms which are at the frequency Ω are preserved. This step illustrates one of the oddities of Mathematica. Strangely, taking the real part of this expression, which is already real, does more to simplify it than does the `Simplify` function. C'est la vie.

```
IntΩ[laser_] =
 Chop[Simplify[Re[Select[Int, ((MemberQ[#, Exp[ I t Ω]] || MemberQ[#, Exp[ - I t Ω]]) && FreeQ[#, w]) &]] /
    Cos[t Ω]]]
For[i = -imax, i ≤ imax, i++, For[j = -jmax, j ≤ jmax, j++, T[i][j] = Exp[-δ[laser + i w + j Ω]]]]
```

Figure A.4: Step Four– Demodulate at frequency Ω.

We can now insert whatever transmission function we desire. A single gaussian makes it easy to see what effect varying `m1`, `m2` or Ω has. We can also use the full absorption of the 1283nm transition, with correct relative amplitudes and frequency spacing and variable gaussian widths to see what we should expect from the lock-in in either the vapor cell or the atomic beam. The full spectrum in this case is a sum of gaussians; this is exactly correct for the atomic beam, but we should remember that the vapor cell actually has a Voigt profile. Nevertheless, because the pressure broadening is small compared with the doppler broadending, the gaussian approximation gives us a good idea of what to expect in the vapor cell.

Using this simulation program, we can see the effects of relaxing each of the assumptions listed at the beginning of this Appendix.

From these plots, one can immediately see that "small modulation index approximation" is untenable. The data shown in Figure 5.1 clearly show second order sidebands and hints of third order ones. Therefore we must also include these terms in our fitting routines. Because of Mathematica's symbolic manipulation abilities, we can calculate the Bessel function and frequency dependencies of the demodulated spectrum including all terms out to third order. We use these results in our fitting routine discussed in Chapter 5.

Appendix B

Laser Multipass

We plan to pass the laser through the atomic beam multiple times for the simple reason that this increases the optical depth by the number of passes, thus increasing the overall sensitivity of our apparatus. The basic idea is that mirrors reflect the laser back and forth as many times as possible.

Figure B.1 shows several possible means of reflecting the laser through the atomic beam. In all cases, the laser "walks" across the two mirrors, with the number of reflections determined by the adjustable angle between the faces of the two mirrors and the laser input angle. We have yet to determine whether it is better for the laser to retrace its steps as it does in plan A at left or to exit via a different face. A practical problem of having the laser retrace its route back out is that the input and output beams end up superimposed, making it more difficult to send the output to the photodiode detector. Most likely, we will permanently mount a mirror on the far side of the atomic beam unit directly to the "output" window extender. Since we have good confidence that the vacuum chamber and window extenders were machined carefully, this will ensure that the mirror face is perpendicular to the beam path, removing the potentially problematic variable of ensuring the far mirror is square with the atomic beam. If we decide to mount the mirror directly to the vacuum chamber in this way, then it will obviously be impossible for the laser to exit through that same port; in that case plan B is ruled out.

Regardless of which design is chosen, it will probably be helpful to align a HeNe reference on top of the diode laser path using a dichroic mirror. This would ease alignment of the multipass mirrors and also make it easier to count how many passes through the atoms the laser makes before going to the detector.

B.1 Problems Discussed

We have considered several systematic errors that might arise as a result of the multipass configuration, but none of them appear to be of great concern. Nevertheless, I will mention them briefly.

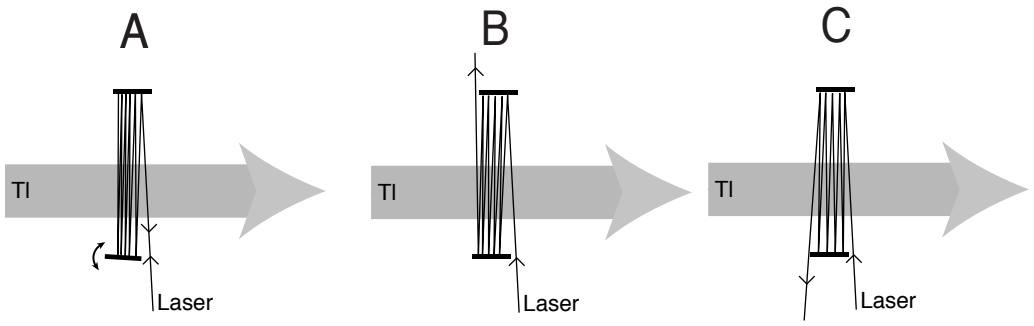

Figure B.1: Three possible configurations for the laser multipass system.

Uniformity of the Electric Field–

As the laser "walks" horizontally through the atomic beam on consecutive passes, one might worry that the applied static electric field or the zeroed magnetic field were non-uniform. Note, however, that the laser already passes through the entire two centimeter width of the atomic beam in the interaction region. Because the entry and exit windows of the ABU are less than one centimeter in diameter, the multipass cannot extend over a horizontal distance greater than this. Thus the laser is already interacting with the atoms over a distance greater than the multipass will introduce, so any field inhomogeneities between passes will be *smaller* than those already present in one pass.

Gaussian Broadening–

If each pass of the laser through the interaction region makes a different angle with the atomic beam, then it will see a different line-of-sight atomic velocity, i.e. the Doppler shift will be different for each pass. Therefore the cumulative absorption profile after multiple passes will be a sum of several gaussians displaced in frequency according to the Doppler shift of each pass. The concern that arises is whether it is still appropriate to fit the final absorption data with a gaussian profile. In fact, this is only a problem if there are just a two or three passes or if the input angle of the laser is far from normal to the atomic beam.

To simulate the errors of fitting several superimposed and displaced gaussians, we fit and collected residuals for several such curves, using Mathematica's nonlinear least squares algorithm. In each case, we added several gaussians with width 40, the FWHM in MHz of the atomic beam, and height 1. We can place an upper limit on the misalignment of the laser input beam by supposing that it traverses the entire width of the input window in one reflection (two passes). Any greater misalignment would mean that the laser would not exit after the second pass. Thus the laser must be perpendicular to within 0.75cm over 80cm of longitudinal travel, or 1.07°. For atoms travelling at 370m/s and interacting with light with 1283nm wavelength, the maximum possible Doppler shift is ±5.4MHz. If we then reflect the beam back on

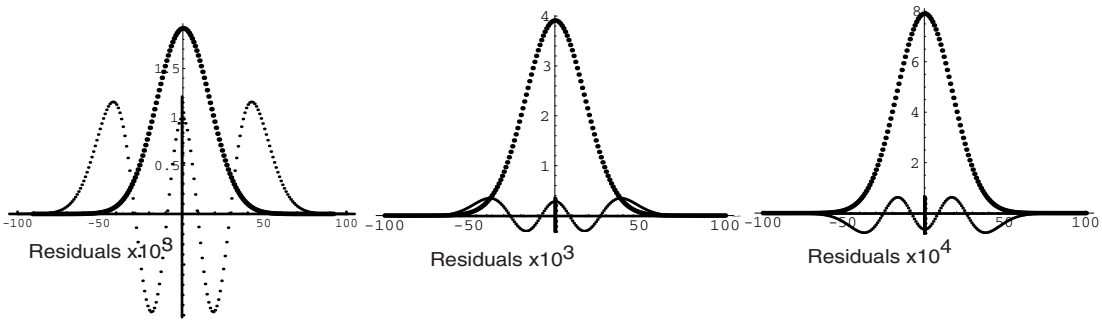

Figure B.2: Lineshapes and fit residuals for superpositions of 2 (left), 4 (center) and 8 (right) displaced gaussians.

itself, then the Doppler shift will be 5.4MHz with the opposite sign. The lineshapes that we fit are composed of either 2, 4 or 8 gaussians, where the maximum Doppler shift in each is ±5MHz. As we add more gaussians, simulating the effect of greater numbers of laser passes, we add gaussians with smaller Doppler shifts. As one adds more passes, the total lineshape becomes more gaussian, as indicated by the rapidly decreasing fit residuals in Figure B.2. We anticipate eventually using a multipass configuration of 10 or more passes, so any deviation from a gaussian lineshape should be less than one part in 10^4, and therefore unimportant.

Bibliography

[CDL77] C. Cohen-Tannoudji, B. Diu and F. Laloe. *Quantum Mechanics*. Wiley, 1977.

[Cor86] Alan Corney. *Atomic and Laser Spectroscopy*. Oxford U. Press, 1986.

[Dem98] Wolfgang Demtröder. *Laser Spectroscopy*. Springer, 1998.

[DBC94] D. DeMille, D. Budker, E.D. Commins. "Measurement of the Stark-induced amplitudes of the $6P_{1/2} \rightarrow 7P_{1/2}$ transition in atomic thallium." *Phys. Rev. A*, December 1994.

[Dor02] S. Charles Doret *A Precise Measurement of the Stark Shift in the Thallium $6P_{1/2} \rightarrow 7S_{1/2}$ 378 nm Transition.* Bachelor's Thesis, Williams College, 2002.

[DFS02] S.C. Doret, P.D. Friedberg, A.J. Speck, D.S. Richardson, P.K. Majumder "Measurement of the Stark shift in the $6P_{1/2}$- $7S_{1/2}$ 378-nm transition in atomic thallium." *Phys. Rev. A*, November 2002.

[Fri01] Paul D. Friedberg. *Measuring the Stark Shift in the $6P_{1/2} \rightarrow 7S_{1/2}$ 378 nm Transition in Atomic Thallium.* Bachelor's Thesis, Williams College, 2001.

[GLW57] R.L. Garwin, L.M. Lederman, M. Weinrich "Observations of the Failure of Conservation of Parity and Charge Conjugation in Meson Decays: the Magnetic Moment of the Free Muon" *Phys. Rev.*, 105:1415, 1957.

[Gol48] Stanford Goldman. *Frequency Analysis, Modulation and Noise* McGraw-Hill, New York, NY, 1948.

[Gri95] David Griffiths. *Introduction to Quantum Mechanics.* Prentice Hall, 1995.

[Her93] G. Hermann, et al. *Z. Phys. D: At., Mol. Clusters* 28, 127, 1993.

[JCG86] G.R. Janik, C.B. Carlisle, and T.F. Gallagher. "Two-tone frequency-modulation spectroscopy." *J. Opt. Soc. Am. B* 3, 1070-1074, 1986.

[KPJ01] M.G. Kozlov, S.G. Porsev, W.R. Johnson. "Parity Non-Conservation in Thallium" *Phys. Rev. A*, 64:052107, November, 2001.

[LY56] T.D. Lee and C.N. Yang "Question of Parity Conservation in Weak Interactions" *Phys. Rev.*, 104:254, 1956.

[MT99] P.K. Majumder and Leo L. Tsai. "Measurement of the Electric Quadrupole Amplitude within the 1283 nm $6P_{1/2} \rightarrow 6P_{3/2}$ Transition in Atomic Thallium." *Phys. Rev. A*, 60:267-272, July 1999.

[Maj03] Protik K. Majumder Private Communications, 2003.

[New01] New Focus, Inc. *Practical Uses and Applications of Electro-Optic Modulators.* San Jose, CA, 2001.

[Nic98] Peter C. Nicholas. *Design and Construction of an Atomic Beam Apparatus for Precise Spectroscopy of Thallium.* Bachelor's Thesis, Williams College, 1998.

[RLM00] D. S. Richardson, R. N. Lyman, and P.K. Majumder "Hyperfine splitting and isotope shift measurements within the 378 nm $6P_{1/2} \rightarrow 7S_{1/2}$ transition in atomic thallium. *Phys. Rev. A*, July 2000.

[Spe00] Andrew J. Speck *Measuring the Stark Shift in the Thallium* $6P_{1/2} \rightarrow 7S_{1/2}$ *378 nm Transition.* Bachelor's Thesis, Williams College, 2001.

[Tsa98] Leo L. Tsai. *Precise Measurement of the Electric Quadrupole Amplitude Within the* $6P_{1/2} \rightarrow 6P_{3/2}$ *Transition in Atomic Thallium.* Bachelor's Thesis, Williams College, 1998.

[Vet95] Paul A. Vetter *High Precision Measurement of Parity Nonconserving Optical Rotation in Atomic Thallium.* Ph.D. Thesis, University of Washington, 1995.

[Yan57] C.N. Yang *The Law of Parity Conservation and other Symmetry Laws of Physics.* Nobel Lecture, December 1957.

[WA57] C.S. Wu, E. Ambler, et al. "Experimental Test of parity conservation in beta decay." *Phys. Rev.*, 105:1413, 1957.

Acknowledgments

This thesis is as much a product of others as myself. I am surrounded by wonderful people who helped me throughout the past year and many since long before I embarked on this project. My parents and sister have supported me in myriad ways and never asked how my experience will get me a job. (Answer: I'm still not sure.) Jesse Dill, Sarah Nichols, Nina Trautmann and Bill Rufus, among others, kept me laughing, smiling and sane with their distractions from work and support for random acts of deviance. I appreciate all those who cared enough to ask how my research was going, and even more those who listened to the answer.

I owe a great debt to my predecessors in the laboratory, only some of whom I know. They aided this work directly, through construction of the apparatus, and indirectly, through the tips and tidbits that have helped us know what to try when stuck. Even their *very* dated dance remix CDs helped on some late nights in the laboratory. Michael Green has made the laboratory more fun through the long winter months and pushed the project along. It goes without saying that Professor Tiku Majumder belongs here, but it must be said that he is a great advisor, steadily pushing me forward, sympathetic to my non-physics interests, always happy to talk and explain things yet again, and exuberant through it all.

To all these people and others, *Thank You.*